

POLITECNICO DI TORINO

SCUOLA INTERPOLITECNICA DI DOTTORATO

Doctoral Program in Electronic Devices

Final Dissertation

**Nanostructured carbon/silicon
composite opto-electrochemical devices
for sensing and energy harvesting
applications**



Dario Imbraguglio

Tutor
prof. Fabrizio Candido Pirri

Co-ordinator of the Research Doctorate Course
prof. Giovanni Ghione

28/02/2013

POLITECNICO DI TORINO

NANOTECHNOLOGIES AND NANOSTRUCTURED
INNOVATIVE MATERIALS

Doctoral Program in Electronic Devices

Final Dissertation

**Nanostructured carbon/silicon
composite opto-electrochemical devices
for sensing and energy harvesting
applications**



Dario Imbraguglio

to my late mother

Contents

Preface	7
Abstract	9
1 Nanotechnologies and nanostructured innovative materials	11
1.1 Porous silicon	13
1.2 Porous silicon-based optical interferometric sensors	17
1.2.1 The Bruggeman's effective medium approximation model	17
1.2.2 Reflectometric interference Fourier transform spectroscopy (RIFTS)	18
1.2.3 Biosensing	22
1.3 Stabilization chemistries of porous silicon	25
1.4 Nanostructured carbon/silicon hybrid devices	29
1.4.1 Supercapacitors	29
1.4.2 Next-generation high-capacity lithium ion batteries.....	32
1.4.3 Porous silicon/carbon composite opto-electrochemical sensors.....	35
2 Fabrication and characterization of porous silicon/carbon composite opto-electrochemical sensors	38
2.1 From silicon to porous silicon	39
2.1.1 Four-point probe measurements of wafer resistivity	39
2.1.2 Electrochemical etching of crystalline silicon	40
2.1.3 The spectroscopic liquid infiltration method (SLIM).....	42
2.2 From porous silicon to carbonized porous silicon	45

2.2.1	The original carbonization procedure	45
2.2.2	Ozone oxidation and furfuryl alcohol infiltration.....	46
2.2.3	Thermal polymerization and carbonization	47
2.3	Porous silicon/carbon coupled opto-electrochemical sensors	51
3	Experimental results.....	53
3.1	Tuning the carbon content and preliminary stability tests	55
3.2	Electrochemical measurements of double-layer capacitances	61
3.3	Coupled opto-electrochemical biosensing	65
3.3.1	Positively charged biomolecules	67
3.3.2	Negatively charged biomolecules	72
Conclusions	76	
References	77	
Acknowledgements/Ringraziamenti	86	
PhD Publications and Awards	88	

Preface

The initial experimental activity of my PhD research project has been carried out at the Istituto Nazionale di Ricerca Metrologica (INRIM) in Turin, Italy. Here, under the supervision of Dr. Luca Boarino and Dr. Andrea Mario Rossi, I worked on two main distinct topics:

- Nanofabrication and characterization of silicon structures obtained by metal-assisted chemical etching and nanospheres' self-assembly;
- Electron beam lithography on electrochemically etched porous silicon as functionalization method for biotechnological applications.

So far, both efforts led to two publications on peer-reviewed journals, which are listed below:

- Boarino L, Imbraguglio D, Enrico E, De Leo N, Celegato F, Tiberto P, Pugno N, Amato G: **Fabrication of ordered silicon nanopillars and nanowires by self-assembly and metal-assisted etching.** *Physica Status Solidi a-Applications and Materials Science* 2011, **208**:1412-1416.
- Imbraguglio D, Giovannozzi AM, Nastro A, Rossi AM: **Submicron machining and biomolecule immobilization on porous silicon by electron beam.** *Nanoscale Research Letters* 2012, **7**:530.

The present thesis, instead, is entirely focused on recent studies conducted during the final third year of my PhD at the University of California, San Diego (UCSD), under the supervision of Professor Michael J. Sailor. The subjects of such a research were also intended to be transferred to the silicon-based nanosystems concerned in the two topics mentioned above, i.e. silicon nanowires and porous silicon, in order to improve their physical-chemical properties and functionalization skills.

Abstract

My research activity deals with fabrication, characterization and functionalization techniques of silicon-based nanostructures and systems, such as silicon nanowires and nanostructured porous silicon. In particular, I focused my final dissertation thesis on the synthesis and study of a new class of carbon/silicon nanocomposites, produced by a recently discovered carbonization chemistry of porous silicon. Such a new chemistry has been optimized in order to obtain samples amenable for applications into a liquid dynamic environment. The employed carbon nanocasting process provides both a stable and conductive hybrid nanomaterial, allowing the carbonized porous silicon film to act as working electrode in aqueous media. The electrode stability has been tried out in different liquids as well as under voltage applied. Moreover, the optical properties of the nanostructure enable its use as a sensor for electrically charged species in buffer solutions, such as biomolecular complexes. By application of an electrical potential difference between the working and a counter electrode, the sensor is able to simultaneously attract and detect both positively than negatively charged targets. In the case of electroadsorbed biomolecules, indications on the retention of their functional activity after releasing from the electrode surface are also provided. Furthermore, an electrical measurement system has been added to the optical one in order to monitor, in real-time with the optically transduced signal, the current flowing between the two electrodes during the sensing experiments. A few prototypes which synchronize the optical and electrical responses of the sensor have been fabricated and their performances tested by varying the electrical parameters. These new combined opto-electrochemical

devices can potentially find applications both in future label-free sensing than in next-generation energy harvesting technologies.

1 Nanotechnologies and nanostructured innovative materials

Nanotechnology is by now a very well-established and productive branch of applied science to modern technological research. Nowadays, the achievement of technical mastery in matter manipulation at the nanometer scale is regarded as the essential requirement for the future development of new generation, advanced technological devices. Over the years, such an acquired awareness has been particularly consolidated by significant breakthroughs on the field of the so-called nanomaterials, i.e., materials with special and distinguishing properties arising from morphological features on an atomic or molecular scale.

Nanomaterials and nanostructures do not typically obey the same laws as macroscopic systems and, on the other hand, they are not microscopic ones (i.e., single atoms or molecules). In such an intermediate (mesoscopic) dimensional range, usually comprised between 2 nm and 50 or even 100 nm, quantum mechanical effects become relevant, as well as functional for potentially revolutionary applications like spintronics or quantum computing. In so far as more pressing technological advances are today demanded, as in the renewable energy sector, the other most important property of these systems can be exploited, that is the vastly increased ratio of surface area to volume present in these materials. For instance, in photovoltaics and power harvesting technologies, a high specific surface area is oftentimes desirable in order to collect or store, respectively, an as much large amount of energy as possible. Besides, the size of these structures is typically

comparable with that of biomolecules and other chemical compounds, thus further extending applications to more interdisciplinary fields, like nanomedicine, sensing or bioelectronics. To date, a flood of devices based on different nanostructures has been proposed and realized for a variety of customized purposes, and a holistic approach of research into materials has matured.

Silicon is still at present the element at the basis of modern consumer electronics, as well as of 1st and 2nd generation commercial solar cells. As a consequence, the current interest on the onward and upward research into silicon-based nano structures and materials is even higher. Depending on the use, different configurations of nanostructured silicon, as in form of particles, wires or tubes, have been proposed and realized. Among these, one of the most studied and versatile is known as porous silicon (PS).

1.1 Porous silicon

PS can be thought as a silicon-based “sponge”, whose morphological features can be tailored according to the specific function it has to fulfill (Figure 1-1). It is commonly generated by electrochemical, stain or metal-assisted etching of crystalline silicon in aqueous or non-aqueous electrolytes containing hydrofluoric (HF) acid. In particular, if the electrochemical or the photoelectrochemical methods are adopted, the size and shape of the pores, the porosity (i.e. the ratio between the volume of voids and the total volume of PS), and its thickness can be easily controlled by varying parameters such as the current density, the etching time, the HF concentration, or the illumination intensity. Also depending on type and doping level of the original silicon starting wafer, different kinds of porous structures can be produced, covering an extensive range of pore sizes which spans from the macro- to the microscale (< 2 nm).

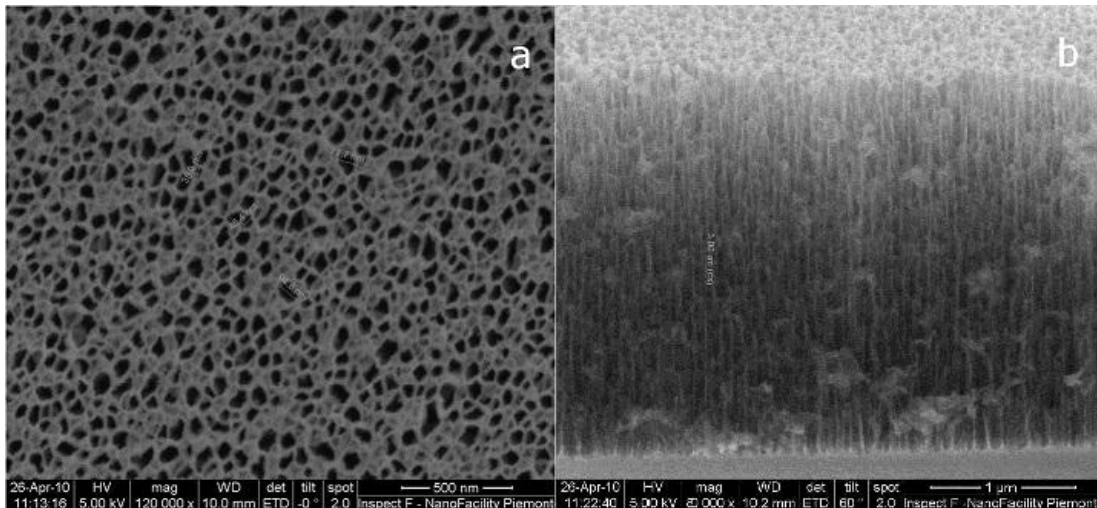


Figure 1-1 Scanning electron microscope top (a) and cross-sectional (b) views of a PS sample.

After its official discovery in 1956, PS took a long time before arousing great attention from the scientific community, which happened just in the early 1990s. Before that time, the uses explored for PS were limited, for example, to the

fabrication of insulating [1] and metal [2] layers on silicon substrates or for vapor sensing applications [3]. The turning point came with Leigh Canham, who first observed efficient, multicolor, room temperature photoluminescence from the material [4]. Almost simultaneously and independently, Ulrich Goesele and Volker Lehmann reported their results about the widening of the PS energy band gap because of quantum confinement effects [5].

Quantum confinement effects (e.g the Coulomb blockade [6]) take place in PS when the diameters of the pores become large enough to extrude low dimensional silicon crystallites. Bulk silicon itself is an indirect semiconductor with a relatively small band gap energy of 1.1 eV (near-infrared). For this reason, bulk silicon does not efficiently emit light and the photoluminescence is observed only at low temperature, which makes unpractical its use in optoelectronic circuits and devices. III-V semiconductors-based rather than silicon ones were considered for applications like light-emitting diodes or semiconductor lasers, which require direct band gap semiconductors in order to have an efficient generation of photons. Hence, the findings of Canham, Goesele and Lehmann represented the possibility to expand silicon technology from micro- to optoelectronics. Unfortunately, some stumbling blocks related to the nature of the material (chemical and mechanical instability, low electroluminescence efficiency, poor electrical transport) somewhat inhibited the research in this field. PS, however, inspired research into a huge number of different applications, and many devices based on PS, such as solar cells, photodetectors, switches, displays, 1-D photonic crystals (“rugate filters”) or more complicated photonic structures (Bragg reflectors, microcavities, optical gratings and waveguides), have been proposed and demonstrated during the years.

Despite luminescence still remained one of the most important characteristics of PS ever investigated, the present-day research on PS focus, instead, on other properties of the material. For instance, in very recent years, the huge internal surface area (which, in PS, can be widened from 10 up to even 1000 m²/cm³) reawakened enormous interest in energy harvesting technologies, since it can be potentially harnessed to produce high-capacity lithium ion batteries (LIBs) of next-generation. In addition, the tunable surface area of PS is reactive enough to allow for an expanding repertoire of wet chemical functionalization techniques [7]. From the past, a well-established modification chemistry has been developed to selectively bind large amounts of different target analytes within the pores and, to date, just about any surface termination can be achieved in PS upon demand. This, of course, has important implications in sectors like the *in vivo* drug delivery, where two other properties of PS turn out to be crucial, i.e. the biocompatibility and the biodegradability. In this case, the use of PS as drug loading/delivery or imaging material relies on its ability to degrade into harmless, biocompatible constituents. A very active and promising research branch that has to be mentioned makes use, to give an example, of PS micro and nano particles, which are able to host and locally release drugs conceived for a specific disease [8].

Finally, the ability to control in a nanometric range the morphological features of PS, such as the size of its pores, adds to the other characteristics of the material, and it found large applications in sensing. A number of highly sensitive and selective both chemical and biological sensors, all based on single- or multi-layered PS films, emerged during the years. In particular, a novel class of PS-based optical interferometric sensors derived from a very fruitful collaboration between the groups of Sailor and Ghadiri [9, 10]. In the next section, the fundamental concepts of

interferometric sensing with PS optical films will be illustrated, since this is one of the two (the main) transduction methods used by the opto-electrochemical devices described in the present thesis.

1.2 Porous silicon-based optical interferometric sensors

The working principle of an optical interferometric sensor based on PS rests on monitoring characteristic changes in the refractive index of the porous matrix, occurring when an analyte-containing or bare medium fills its pores.

1.2.1 The Bruggeman's effective medium approximation model

Being substantially a mixture of silicon and air, pristine PS is a two-phase composite, and its refractive index is thus expected to be lower than that of bulk silicon. Nevertheless, the direct determination of the refractive index (dielectric function) of a PS layer is not an easy task, since it must take into account both the individual constituents, i.e. the silicon skeleton and the medium filling the void spaces within the pores (e.g. air), and the porosity of the film. Therefore, an “effective medium approximation” must be used in order to estimate the optical constants of PS. Among the existing theories, the Bruggeman's model has been shown to predict porosity and thickness of PS samples in good agreement with gravimetric determinations [10-12], and it is one of the most used. An example of how the “effective” refractive index n of a PS film can be calculated, by averaging the refractive indexes of the distinct components in a Bruggeman's picture, is given by the following relationship [10], in the general case of any (gaseous or liquid) filling medium:

$$n = \frac{1}{2} \sqrt{2n_S^2 - n_M^2 - 3Pn_S^2 + 3Pn_M^2 + \sqrt{8n_S^2 n_M^2 + (n_M^2 - 2n_S^2 + 3Pn_S^2 - 3Pn_M^2)^2}}$$

where n_S is the wavelength-dependent refractive index of the silicon skeleton of the porous matrix, n_M is the wavelength-independent refractive index of the medium filling the pores, and P is the porosity.

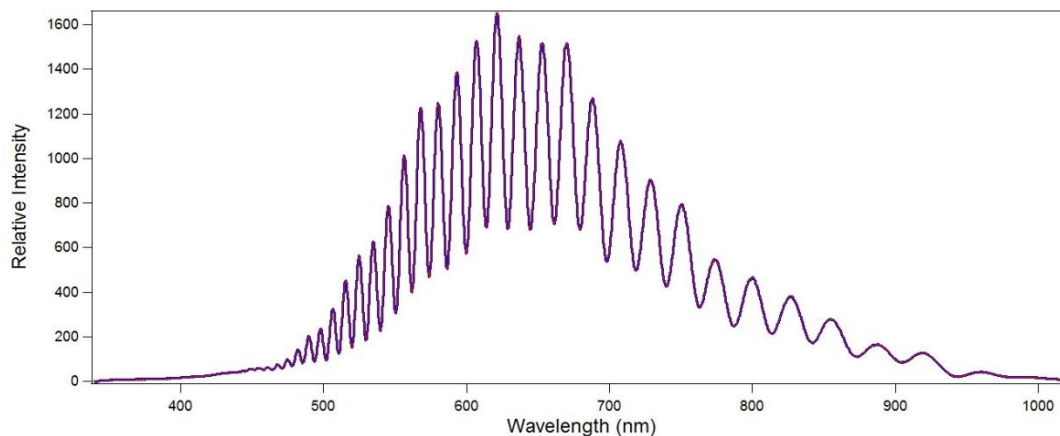


Figure 1-2 Reflected white light spectrum collected in air of a PS sample.

1.2.2 Reflectometric interference Fourier transform spectroscopy (RIFTS)

Interferometric optical sensing with PS is obtained through the so-called RIFTS (reflectometric interference Fourier transform spectroscopy) method [13-19]. Such a technique takes advantage of the fact that illumination of sufficiently narrow-sized porous samples causes multiple reflections of light at the interfaces of PS layers. In the particular case of a single layer, the interfaces are just two: the upper one between medium and PS and the lower one between PS and the underlying silicon bulk. This phenomenon results into constructive and destructive interference effects which lead to the formation of a regular interferometric optical pattern (Fabry-Pérot fringes). For a PS-based sample to display Fabry-Pérot fringes, the layer must be flat and reflective and the pores much smaller than the light wavelength (~ 500 nm), otherwise incoherent light scattering will dominate the interference spectrum. Since the PS samples intended for the present work are mesoporous (i.e. with a disordered

distribution of pore sizes comprised between 2 and 50 nm) single layers, they exhibit an optical interferometric pattern like the one of Figure 1-2, which has been reported as representative example.

The Figure 1-2 shows the raw reflected light spectrum in air, plotted in terms of wavelengths, of an as-etched PS sample. The sample was illuminated with focused white light, and reflected light was collected through the same lens positioned along an axis normal to the PS surface and then transmitted to a CCD-based spectrometer. The RIFTS method applies a fast Fourier transform (FFT) algorithm to the frequency spectrum associated with the input waveform of Figure 1-2, enabling to extract the basic optical parameters of the PS film. The raw spectra of Figure 1-2 were therefore inverted in units of frequency in order for the Fabry-Pérot fringes to be periodic, the data interpolated to be evenly spaced, and the resulting reflectance spectrum was transformed by a digital FFT. This computation yields a peak whose position and intensity is directly connected to the PS optical constants. An example of the FFT of the reflectance spectrum of a single layer Fabry-Pérot PS film is reported in Figure 1-3.

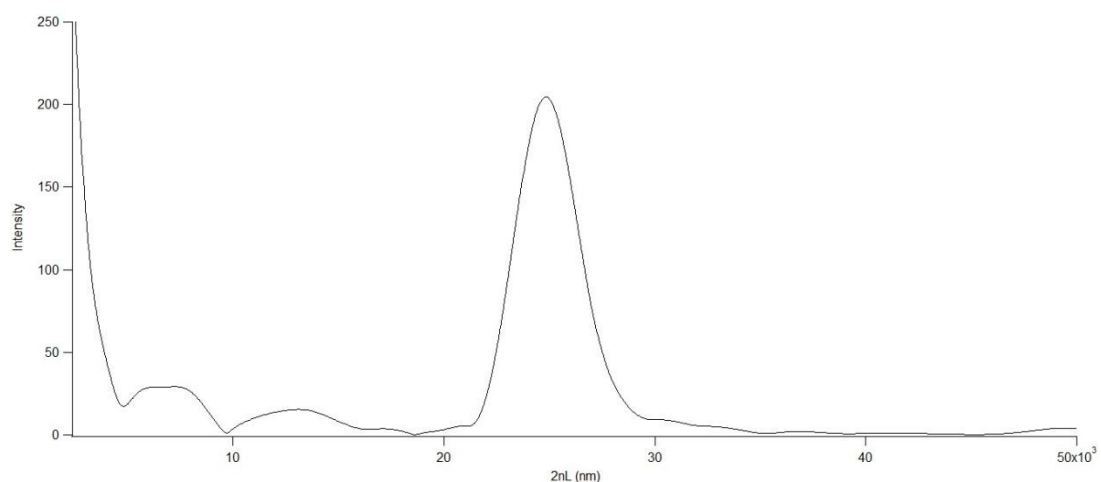


Figure 1-3 Corresponding Fourier transform of spectrum from Figure 1-2.

The peak in Figure 1-3 has been obtained from the spectrum of Figure 1-2 by application of the FFT in the range comprised between 600 and 1000 nm, which is the typical operational spectral window (for untreated PS samples) to avoid errors due to optical absorptions by the PS film at shorter wavelengths. The position of the peak along the x -axis is equal to the quantity $2nL$ (product of the effective refractive index n and the physical thickness L of the single layer) and is determined via the Fabry-Pérot relationship:

$$m\lambda = 2nL$$

where λ is the wavelength of maximum constructive interference for a spectral fringe of order m while the factor of 2 derives from the 90° backscattering configuration of the illumination source and detector. The term $2nL$ is thus the optical path length, hereafter referred to as the effective optical thickness (EOT) of the PS film.

The EOT in air of the PS sample reported by way of example in Figure 1-3 is 24848.2 nm. If a liquid medium is admitted into the void spaces within the pores, the effective refractive index n of the PS layer will increase, producing a spectral shift in the Fabry-Pérot fringes and a corresponding change in the computed value of the EOT. Since liquids have higher refractive indexes than air, the shift will be towards higher wavelengths and it is commonly referred to as redshift. On the contrary, in case of decrease of the EOT, the notation used will be blueshift.

The EOT, and in particular its continuous monitoring as a function of time, can provide combined information on the morphological evolution of a PS matrix (physical thickness L) in respect of the specific liquid medium it is immersed in (effective refractive index n). In order to allow comparisons between different samples and liquids, the percentage change in the EOT has to be considered:

$$\% \Delta EOT = \frac{EOT_t - EOT_{t=0}}{EOT_{t=0}} \times 100$$

where EOT_t and $EOT_{t=0}$ are measured at a given time t and at the initial time $t = 0$, respectively. Therefore, in the ideal case of a PS sample completely stable in the liquid environment it is in contact with, with no other interferences perturbing the system, the profile of the $\% \Delta EOT$ as a function of time will be simply represented by a straight horizontal line parallel to the temporal x -axis and centered at the 0 value along the y -axis. On the other hand, deviations from this value (or from a given reference baseline) will be detected when the optical constants of PS change due, for instance, to admission into the pores of a specific analyte during a sensing experiment.

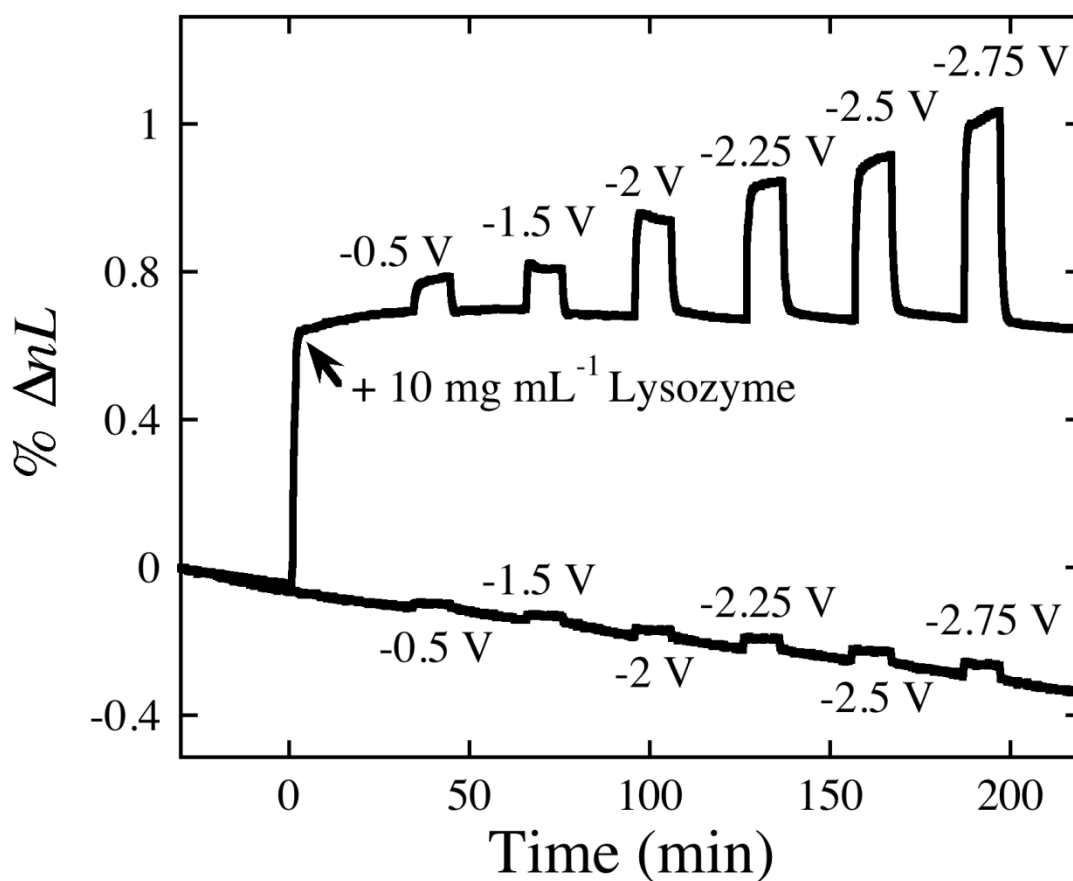


Figure 1-4 Percent variation in nL as function of time of a PS optical film with (upper trace) and without (lower trace) introduction of 10 mg mL^{-1} lysozyme at $t = 0$. Taken from reference [20].

1.2.3 Biosensing

A demonstrative example of the sensing mechanism of a PS optical film is illustrated in Figure 1-4. As previously mentioned, the mesoporous samples of the present thesis have pore diameters which fall in the range 2-50 nm. Many proteins, enzymes and antibodies have dimensions of the order of 10 nm; thereby, being the porous material able to act as analyte capture matrix, meso-PS-based devices find a natural application as biosensors. In the reported work [20], Chen and coworkers achieved electric-field-assisted transport, capture, and interferometric sensing of biomolecules by using a chemically modified (see following sections) nanostructured optical film of meso-PS. Electroadsorption was applied as analyte capture method, allowing the device to simultaneously attract and detect (in buffer solutions) electrically charged proteins, by application of an electrostatic potential opposite to their surrounding one. A phosphate buffer saline (PBS) solution containing positively charged lysozyme was circulated through the film, and a negative bias was applied in a series of discrete steps to the PS-based sample in order to move and adsorb the biomolecules to the pores walls. Bias was maintained at a given value (from -0.5 to -2.75 V) for a total of 10 min, after which it was each time set back to the 0 V initial value for 20 min. The Figure 1-4 reports the optical response of the sensor monitored as a function of the time and the voltage provided. In this case, the percentage change in the EOT was calculated through the formula:

$$\% \Delta nL = \frac{nL_{t,\Delta V} - nL_{t=0,\Delta V=0}}{nL_{t=0,\Delta V=0}} \times 100$$

where $nL_{t,\Delta V}$ was measured at a given time t and applied bias ΔV , while $nL_{t=0,\Delta V=0}$ was the value of nL measured from the sample in pure buffer solution at a time immediately prior to introduction of protein ($t = 0$) and at an applied bias (ΔV) of 0 V

relative to a platinum counter electrode. The upper trace of Figure 1-4 shows the measurement carried out in the presence of biomolecules, whereas the lower one is the control obtained in pure PBS. As one can see by comparing the initial baselines of the two traces, introduction of lysozyme resulted in an instantaneous increase in the value of $\% \Delta nL$ as long as the proteins infiltrated the PS matrix. After a new steady-state value was reached, the film was held at a negative potential and a further increase in $\% \Delta nL$ was observed, which was consistent with the electroadsorption of the biomolecules. The release of lysozyme was easily achievable by setting a 0 V bias: the $\% \Delta nL$ returned to the original baseline value as soon as the voltage was set to 0 V. Besides, the amplitude of the $\% \Delta nL$, related to the quantity of adsorbed lysozyme, indicated significant accumulation of the protein within the matrix and it was proportional to the applied bias. Such a voltage-dependent response is evident in the upper trace of Figure 1-4, but it can be also detectable in the control experiment of the lower one. Since the response of the optical biosensor ultimately depended on the analyte mass, the small increases observed in the $\% \Delta nL$ were found to be consistent with the small molecular mass of the cationic species (mainly Na^+) present in the PBS control solutions.

The slow, steady decrease in the baseline value of the $\% \Delta nL$ standing out at a bias of 0 V in pure PBS (low trace of Figure 1-4) is representative of the oxidation and subsequent dissolution of the mesoporous matrix into the aqueous buffer. This is one of the key limitations of optical biosensors based on PS since it leads to a zero point drift and place a fundamental restriction on the ultimate sensitivity of the device. There is a great interest in functional PS surfaces that were enough stable in aqueous media today, which is not only driven by biosensing and drug delivery applications, where hours-to-months endurance is, however, often required. In energy storage

technologies, for instance, the search for new highly capacitive supports that could withstand, without appreciable degradation, to electrolyte exposure for longer-term periods (up to several years) is still an open issue.

1.3 Stabilization chemistries of porous silicon

One of the major barrier preventing commercial applications of PS is the instability of its native surface. Hence, surface chemistry has proven to be a crucial element for the technological success of this material.

Due to the huge surface area, PS is particularly susceptible to air or water oxidation, as well as to contaminations by different types of species which can lightly or heavily affect its properties. As confirmed by Fourier-transform infrared spectroscopy measurements [10, 21], immediately after being electrochemically etched, the surface of PS is covered with a passivating layer of Si–H bonds, with minor quantities of Si–F and Si–O species. Such an as-formed surface is metastable, and it reacts spontaneously with water vapor in the air even at room temperature. As a consequence, a thin oxide (SiO_x) layer will form within timescales of minutes. Anyway, this is largely sufficient for transfer of freshly etched samples into inert-atmosphere glove boxes and Schlenk lines for manipulation via wet chemical techniques [10, 7].

The reactivity of PS is dominated by the chemistries of the Si–H and the Si–Si bonds. Both of these species are able to reduce water, which is a competent oxidant for PS. As already said, even water vapor has sufficient oxidizing potential to spontaneously react, at room temperature, with the PS surface to form Si–O bonds. If such a reaction is performed in liquid water, the nanophase SiO_x can readily dissolve due to hydrolytic attack. Indeed, hydroxide ions (OH^-) attack both Si–H and Si–O surface species and generate intermediates which then induce the Si–Si bond cleavage. Depending on the application, much of the chemistry on PS has been developed to minimize or to harness these oxidation reactions. The chemical functionality of the reactive hydride species in pristine PS provides, however, a

versatile starting point for various reactions that can control the dissolution rate in aqueous media. Presently, two are the most important approaches that have been taken to stabilize PS: the first is to purposely oxidize it, while the second involves the formation of Si–C bonds.

A variety of chemical or electrochemical oxidants and techniques can be used to oxidize PS, such as gas-phase oxidations (like annealing with high-pressure water vapor, rapid thermal oxidation, ozone) or oxidation induced by either cationic surfactants or organic species. The simplest oxidant is air, which produces different types of surface species, according to the temperature at which the reaction is performed and the humidity of the air. At room temperature, the oxide layer grows over the time assisted by stronger oxidants as ozone and nitrogen oxides present in the atmosphere. Anyway, in some cases, the original freshly etched, hydrogen-terminated PS surface can be quickly recovered by dipping the sample in an HF-based solution. Air oxidation of PS is usually performed at high temperatures in order to anneal and stabilize the Si–O bonds. Afterwards, the oxidized material can be further modified using conventional silanol chemistries employed to modify silica (SiO₂) surfaces. However, an electronegative element such as oxygen somewhat enhances the tendency of silicon to be attacked by nucleophiles, and Si–O bonds in oxidized PS are still unstable in aqueous media because of hydrolytic attack. In contrast, the low polarity of Si–C bonded species makes them kinetically inert toward attack by water and hydroxides due to the low electronegativity of carbon.

Several different methods have been developed during the years to produce Si–C bonds on PS surfaces, such as thermal or microwave-assisted hydrosilylation and chemical or electrochemical grafting of Si–C species. Carbon covalently bonded to silicon can impart good stability and a high degree of hydrophobicity to the surface,

providing a means to attach a wide variety of organic functional groups, sufficiently hydrophobic that water is excluded from the immediate vicinity of the attachment point. Si–C bonds are much less polar in respect with Si–O ones, and reactions that form surface Si–C bonds show much greater resistance to attack by nucleophiles. Nevertheless, both hydrosilylation than Si–C grafting suffer from the fact that they do not completely remove all the Si–H species from the surface but rather merely decorate it with functional groups. A number of surface reactive Si–Si and Si–H species remain after the reactions, still accessible to aqueous solution. On the other hand, silicon carbide is a well-known material that can yield very stable surface species. It was this idea that inspired Salonen and coworkers to develop a carbonization reaction for PS similar to those that produce silicon carbides [22].

Salonen's "hydrocarbonized" surfaces are synthesized by high-temperature decomposition of acetylene gas on as-prepared PS [22-24]. In a typical procedure, freshly etched PS samples are thermally carbonized in a tube furnace at 450 °C for 30 min, with a constant flow of acetylene and nitrogen gas. The temperature of the pyrolysis reaction plays a key role in determining the degree of hydrophobicity or hydrophilicity of the samples. The resulting films are composed of an ill-defined mixture of C–H, aromatic C=C, and C–OH species. Generally, they remained enough porous to display Fabry-Pérot fringes for use as optical interferometric sensors, as in case of the one presented in the previous section (Figure 1-4), chemically modified according to the Salonen's procedure [20]. Although less well-defined than material prepared by hydrosilylation and grafting routes, hydrocarbonized PS is environmentally stable and its chemical sensing capabilities have been widely demonstrated [25-37]. Furthermore, Salonen's carbonaceous surfaces provide both conductive and biocompatible supports for protein

electroadsorption/desorption experiments like those performed by Chen and coworkers, which are not possible to achieve by using freshly etched or oxidized PS samples since they are, as well as not enough stable upon immersion in the liquid solutions required by biomolecular complexes, semi and completely electrical insulating materials, respectively. In the case of lysozyme loaded into a hydrocarbonized PS optical sensor at an applied bias $\Delta V = -2.75$ V for 120 min, more than 80% of its enzymatic activity was, in fact, preserved after releasing the proteins into free solution. Thus, this carbonization chemistry opened the door to similar tests not only with different and eventually further functionalized biomolecules (to improve biosensing selectivity and specificity), but also with other electrically charged species for new interesting applications as, for instance, high-performance rechargeable LIBs based on PS.

1.4 Nanostructured carbon/silicon hybrid devices

In the last decade, especially after discovery of graphene in 2004 by Andre Geim and Konstantin Novoselov at the Manchester University, carbon-based nanomaterials and devices drew more attention than others by the scientific community, being still now considered as the best candidates to substitute silicon-based systems in many diverse applications. Most of the various allotropes of carbon share some peculiar properties which can potentially make them new leading materials in different important applied fields, in particular if occurring in a regularly ordered nanostructured arrangement of the carbon atoms. High electrical conductivity and optical transparency (graphene), mechanical strength and flexibility (carbon nanotubes) or even superconductivity (buckminsterfullerenes) are just a few examples of the advantages that these nanomaterials can offer over silicon-based ones [38].

1.4.1 Supercapacitors

Among so many prospects, one of the biggest and hardest challenges facing modern research is to provide new systems able both to store than deliver more and more energy at increasingly high rates. At present, graphitic (i.e. carbon-based) materials are commonly employed as negative electrodes in the conventional LIBs used, for instance, by the telecommunications electronics. Until now, their specific energy and power capabilities turned out to be satisfactory enough to have permitted the development of light in weight, portable and environmentally friendly batteries at an acceptable cost to be commercially available. However, considerable improvements are always more requested not only to decrease energy and time needed to recharge

state-of-the-art high-tech electronic devices, but also to meet the stronger demand of energy storage required in other kinds of mobile or fixed applications, as in full electric vehicles or solar harnessing technologies. In such a view, a very promising answer can be again offered by carbonaceous materials, which are the most investigated ones in order to make the so called supercapacitors [39].

Supercapacitors (also referred to as ultracapacitors) is a generally adopted name for that class of devices capable to achieve energy densities several orders of magnitude higher than traditional dielectric capacitors, having at the same time a power density far larger than common LIBs and fuel cells. Supercapacitors are usually classified into two main categories: (i) redox supercapacitors or pseudocapacitors and (ii) electrochemical double layer capacitors. The basis of energy storage in the former ones is Faradaic charge transfer. The electrical charge is built up via an electron transfer mechanism producing changes in the chemical or oxidation state of the electroactive material, according to Faraday's laws related to the electrode potential. Thus, they are somewhat battery-like in the behavior since the storage of electric charge and energy is not electrostatic in origin (hence the prefix "pseudo") but deriving from electrochemical charge-transfer processes, involving the electrode materials to undergo reversible Faradaic redox reactions during the charge/discharge cycles. Generally used materials in redox supercapacitors are transition metal oxides [40] (RuO_2 , Co_3O_4 or MnO_2 and MnO_3) or electronically conducting polymers [41] (polyaniline, polypyrrole or derivatives of polythiophene) that can exhibit significantly high pseudocapacitances, even though they often suffer of either poor conductivity (metal oxides) or poor stability during cycling (polymers). By contrast, in spite of a lower specific capacitance, carbon can impart at the same time high conductivity and high stability in supercapacitative devices as the electrical double

layers [42-43]. As in common electrostatic capacitors, the energy storage mechanism in these systems is simple charge separation, but resulting from the formation of an electric double layer at the interface between an electronically conductive material and the adjacent liquid electrolyte interposed between the anode and cathode electrodes (also known as the solid-electrolyte interphase). In this case, the charge process is not Faradaic, i.e. ideally no electron transfer takes place across the electrode interface. In respect to conventional capacitors, the vast increase in capacitance achievable by electrical double layer supercapacitors is principally a function of two factors: (i) an extremely small distance separating the opposite charges, as defined by the electric double layer; (ii) highly porous structured electrodes that embody very high surface areas. Contrary to batteries, where charge-transfer and chemical phase changes introduce additional relatively slow steps into the process of energy storage and delivery, the mechanism in electrical double layers is inherently rapid, as it simply involves movements of ions to and from the electrode surface. Since a larger amount of energy can be stored within the pores of high surface area materials, various porous forms of carbon are, therefore, usually preferred. Activated carbons, carbon fibers and carbon aerogels are, to date, the most widely utilized ones. In particular, ordered carbon nanostructures are recently emerging as good candidates to make new supercapacitive devices, since their nanoscale and readily accessible morphology can offer a unique combination of high electrical conductivity and porosity, and shorten the transport path of ions and electrons. As in sensing applications, where the properties of homogeneous carbon nanostructures had been largely explored [44-45], the use as supercapacitive electrodes of carbon nanofibers [46], single- [47] and multi-walled [48] carbon nanotubes and, recently, graphene [49] has been demonstrated. Single-phased carbon

materials and nanostructures can potentially greatly enhance the cycling performances of the anode and thus enormously extending lifetimes and charge/discharge rates of products which make use of rechargeable batteries. Nevertheless, their widespread application is essentially limited by the fact, as mentioned before, that the capacitance values attainable thus far are still lower than those of commercial LIBs.

1.4.2 Next-generation high-capacity lithium ion batteries

As far as traditional LIBs are concerned, a further new research trend aimed to improve their performances has rapidly grown up in the last few years. In a different perspective, heterogeneous nanostructured materials with multi-nanocomponents are proposed [50-56], in order to synergically match the distinguishing properties of the individual constituents. Each component can be, as a matter of fact, tailored to meet different demands, e.g. high energy density and high conductivity. In such a way, energy storage/delivery systems with very high capacitances can be, in principle, fabricated without sacrificing cycle life or high power densities.

The major obstacle to the breakthrough of high-capacity LIBs is to find a reliable replacement to graphite, the negative electrode commonly used in conventional LIBs, which is affected by a limited reversible charge capacity of 372 mA h g^{-1} . Materials forming alloys with lithium (like Sn, Sb, Ge, and Si) are potentially more attractive anode candidates, since they can incorporate larger amounts of lithium ions. Among lithium alloys, silicon is considered to be one of the next-generation anodic materials for LIBs, since it is known to have the highest theoretical gravimetric capacity at $\sim 4200 \text{ mA h g}^{-1}$, a volumetric capacity of $\sim 8500 \text{ mA h cm}^{-3}$, and can offer an appropriate low voltage for an anode.

Silicon reacts with lithium to form binary alloys with a maximum uptake of 4.4 lithium atoms per silicon atom ($\text{Li}_{22}\text{Si}_5$). At room temperature, the highest achievable specific capacity for silicon is 3579 mA h g^{-1} , far greater than the analogous value for graphite. Nevertheless, crystalline silicon suffers from drastic volume changes during lithium alloying (to form Li_xSi) and de-alloying (to reform Si) that has greatly slowed down its application in this field. Upon insertion of lithium ions (lithiation), silicon can expand volumetrically even up to 400% with anisotropic elongation along the $\langle 110 \rangle$ direction, and it can contract significantly with the subsequent extraction (delithiation). Repeated lithium insertion/extraction cycles invariably generate great mechanical stress in the brittle silicon crystal lattice, leading to severe cracking that makes the silicon electrodes lose contact with the current collector. Capacity fading and pulverization of the structure are the consequences of such a gradual destruction, which finally results in poor cyclability or even completely failure of the electrode. Anyway, reducing the material size to the sub micrometer or nanometer range can somewhat solve the problem mentioned above. Indeed, the internal strain in incompact silicon nanostructures can be easily relaxed, without mechanical fracture, because of their small size and the free surrounding space that becomes, consequently, available.

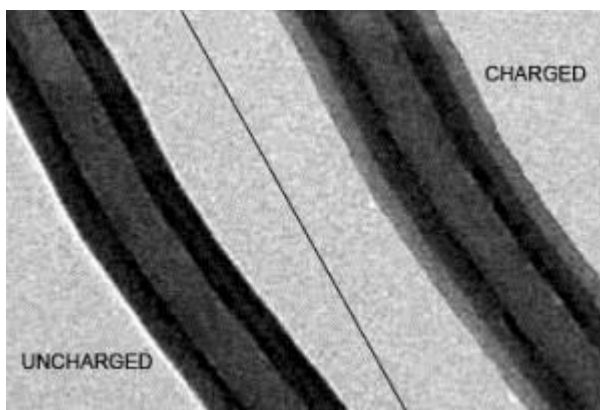


Figure 1-5 Real-time in-situ transmission electron microscopy images of a carbon/silicon nanocomposite during lithium charging/discharging cycles. Adapted from reference [54].

Several different submicron and nano morphologies of silicon have been separately suggested to ease the volume expansions during the lithium ion insertion/extraction cycling, including silicon sub

micrometer pillars, crystalline-amorphous nanowires arrays, nanotubes, nanoparticles, thin films and PS [51-53]. Bare silicon nanostructures, in any case, have two main drawbacks to be applied for LIBs: low electron conductivity (most of all if undoped silicon structures) and low diffusivity for lithium ions. To overcome these kinds of issues, an alternative strategy has been undertaken, i.e. adding a covering layer with functional coating materials. In this case, the goal is, on one hand, to enhance the charge transfer kinetics of the electrode and, on the other hand, protect silicon from generating a solid-electrolyte interphase, thus preventing its decrepitation upon cycling. Among other competitive options, a carbon-based coating can be again a worthwhile choice, due to the good electrical conductivity of carbon and its ability to accommodate silicon volume changes. More importantly, as already stressed [42], the formation of a solid-electrolyte interphase involving a porous carbon material can be, conversely to stark silicon, much more convenient, since its pores are able both to host than furnish rapid access to a large number of ions into the bulk. Furthermore, the additional porosity associated with a carbon matrix can “sum” to the high surface area which can provide a nanomaterial like PS, thus allowing dramatic increases in capacitance. Moreover, despite a more rigid and heavy structure of silicon-based electrodes compared to carbon-based ones (causing increases in the weight of the anode), a silicon skeleton is, most of the time, particularly welcome as it is compatible with standard silicon technology. Otherwise, a reverse configuration can be also expedient. By way of example, Figure 1-5 shows very recently published results [54] about real-time phase transformation investigations of single carbon nanofibers coated with amorphous silicon, made possible by in situ transmission electron microscopy carried out during the charge/discharge processes. Even just considering only silicon- and carbon-based

starting nanomaterials, a plenty of different morphologies, combinations and architectures is conceivable. Each type of composite electrode has its pros and cons and finding the optimal solution is still a great challenge to most of the researchers in this field.

The nanostructuring and nanocomposition approaches briefly overviewed as yet keep showing very encouraging results and might revolutionize future energy technologies as in LIBs, even if the scale-up of these systems is, up to now, still far from meeting industrial levels. In the depicted scenario, however, there is a shortcoming of fast and cheap methods enabling to monitor in real time the structural evolution of nanostructured matrices upon interaction with different testing electrolytes and electrically charged species. From this point of view, a device inspired from the sensing mechanism elaborated by Chen and coworkers [20] (formerly introduced in the subsection 1.2.3) could potentially serve the purpose.

1.4.3 Porous silicon/carbon composite opto-electrochemical sensors

Chen's work could be thought as one pioneering attempt to address the optical capabilities of PS towards the study, upon electrical perturbations, of electrically complicated systems such as biomolecules-containing saline buffer solutions. Although completely oriented to biomolecular sensing, the suggested platform can be, anyway, extended to smaller charged atomic targets as ions.

Chen and coworkers successfully applied the Salonen's thermal carbonization chemistry [22] (see section 1.3) to a PS optical film in order to use it as an electro-adsorptive substrate. The sensor was able to detect (by optical interferometry) positively charged biomolecules, which retained their functional activity after being

released from the electrode surface. Nevertheless, the sensor was not applicable to negatively charged molecules due to a lack of stability of the carbonized PS electrode under positive bias conditions. Since this was not a fundamental limitation of the carbon electrode, the causes of such instability were not further investigated. Anyway, a number of other carbonization chemistries exist which can likewise work inside the nanopores of a PS template. In particular, a very recently emerged one [57] exploits one of the most common methods utilized to generate high surface area carbons, which is pyrolysis of a carbon-containing resin or polymer. With the new discovered technique, Kelly and coworkers took advantage of the peculiar morphological structure of a PS rugate filter to mold the formation of characteristic carbonized PS (CPS) composites, constituted by carbonized bundles of fibers embedded into a periodic PS matrix. When combined with the signal transduction properties of a PS photonic crystal, the film acted as highly sensitive optical vapor sensor for volatile organic compounds. These CPS composites were shown to more strongly adsorb organic vapors (e.g., toluene) than either freshly prepared or ozone-oxidized porous silicon films, and the photonic properties of the rugate filter provided a means to optically detect the adsorption event. Moreover, dissolution of the PS skeleton generated arrays of free-standing glassy carbon nanofibers that replicated the porosity of the template.

To the best of author's knowledge, the stability of CPS composites produced through the Kelly's carbonization chemistry has not been systematically tried out, as yet, neither in aqueous solutions nor under voltage applied. In the present work, Kelly's chemistry has been slightly modified to precisely control the final carbon content in CPS samples, thus making them amenable for optical applications into a dynamic microfluidic apparatus. The optimized procedure to fabricate reproducible CPS

composites will be following described and their characterization will be discussed. The obtained CPS electrodes have been tested under stress conditions in different liquids and polarizing them at different voltages. Due to the natural inclination of PS as biomaterial, however, much of the effort has been spent to develop a highly sensitive and reliable biosensor equivalent to the Chen's one, providing results with both positively than negatively charged biomolecules. Nevertheless, some tests performed in pure saline ionic solutions will be also presented since, still to the author's personal opinion, this aspect deserved more attention. Furthermore, a parallel electrical measurement configuration has been realized to simultaneously acquire, during the sensing experiments, the electrochemical characteristic of the device along with the optical one. New coupled opto-electrochemical sensors are thus proposed to assist more expensive and time-consuming techniques in order to better understanding the real-time behavior and performances of these nanosystems.

2 Fabrication and characterization of porous silicon/carbon composite opto-electrochemical sensors

In this chapter, an overview on the fabrication and characterization techniques of the opto-electrochemical sensors subject matter of the present thesis will be given.

In the first section, the standard procedure to produce the starting PS samples will be briefly summarized. For a complete and more detailed coverage about preparation and characterization of PS optical films and used instrumentation the reader is referred to [10]. The second section is devoted to the realization of CPS composites, with particular attention to the expedients which have been adopted to make them suitable for repeatable optical sensing applications. Lastly, in the third section, the manufacturing of a real sensing device will be illustrated, by both describing the various components than showing the coupled optical/electrical measurement system that has been assembled for the sensing experiments.

2.1 From silicon to porous silicon

All the PS samples presented in this work have been prepared in the same way according to the procedure described in [20], in order to obtain mesoporous single layers with nominal pore diameters = 40 nm, thickness (L) = 9.8 μm , and porosity (P) = 73%.

2.1.1 Four-point probe measurements of wafer resistivity

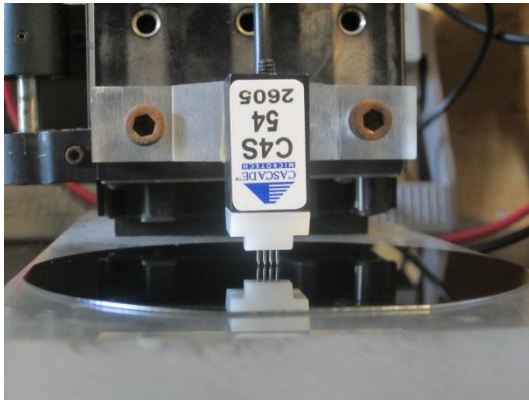


Figure 2-1 A four-point probe head in contact with a silicon wafer during a resistance measurement.

The preparation of PS samples starts from 4" crystalline ($\langle 100 \rangle$ -oriented) boron-doped silicon wafers, in the present case provided from Siltronic Corp. (Figure 2-1). Since the PS films are designed for an

electrochemical use, the check and determination of the effective electrical

resistivity of the pristine material is essential. Such an evaluation can be readily done by a series of four-point probe measurements. A four-point configuration is required in order to overcome contact resistance problems of a two-point one, which are due to the high resistivity of native SiO_x layers present on the surfaces of silicon starting wafers.

A constant current (I) was passed between the outer two tips of the 4-point probe head showed in Figure 2-1, while the voltage drop (V) was simultaneously measured between the two inner ones. Afterwards, the obtained resistance values (V/I) were converted to sheet resistance values (R_S) by the relation:

$$R_S = \frac{V}{I} \cdot CF$$

where $CF = 4.532$ is a correction factor that is related to the sample geometry (infinite sheet approximation). Finally, the resistivity ρ was calculated by the simple formula:

$$\rho = R_S W$$

where W is the measured thickness of the silicon wafer. The Table 1 reports some representative values obtained in different spots of the same silicon wafer ($W = 525 \mu\text{m}$), from which all the PS samples that will be presented in this thesis have been derived.

Table 2-1 Resistance and resistivity values measured on five different spots of a silicon wafer.

	V/I (Ω)	R_S (Ω per square)	ρ (Ω cm)
1	0.004375	0.019828	0.001041
2	0.004370	0.019805	0.001040
3	0.004347	0.019701	0.001034
4	0.004367	0.019791	0.001039
5	0.004325	0.019601	0.001029
Avg	0.004357	0.019745	0.001037

The average resistivity is about $1.04 \text{ m}\Omega \text{ cm}$, which corresponds to a highly doped silicon wafer, often referred to as “degenerately” (p^{++} -type) doped.

2.1.2 Electrochemical etching of crystalline silicon

The silicon wafer was cleaved into smaller squared chips ($1.5 \times 1.5 \text{ cm}^2$), each of which was then electrochemically etched in order to fabricate a mesoporous single layer.

The PS samples were produced by electrochemical anodization of silicon in an HF-based solution, the formation involving reactions of Si-Si, Si-H, Si-O, and Si-F bonds at the surface of the silicon material. For such a type of highly doped/low resistive silicon crystal the etching mechanism is dominated by carrier tunneling [10].

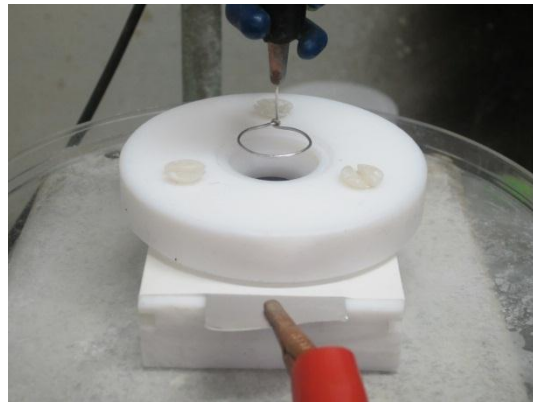


Figure 2-2 A conventional electrochemical cell used to etch PS samples.

A standard single-tank HF-resistant Teflon etch cell is pictured in Figure 2-2. The sample, with a round exposed area of 1.2 cm^2 , was mounted inside the cell using an aluminum foil as back-contact and a platinum loop as counter electrode. In such a two-electrode configuration, the silicon chip serves as the anode. The sample was then anodically etched in a solution of concentrated (48%) aqueous HF in anhydrous

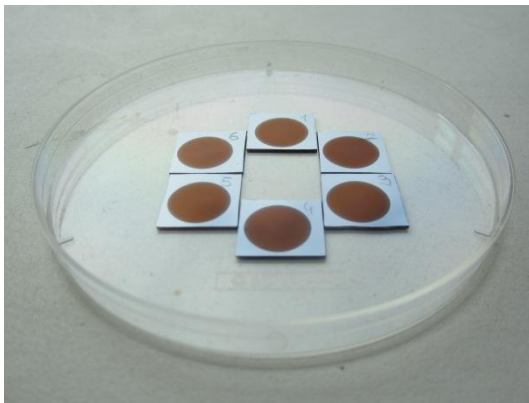


Figure 2-3 As-etched PS samples used in the present work.

ethanol (3:1 v/v HF:EtOH) by application of a current density of 467 mA cm^{-2} for 48 s. Immediately after etching, it was rinsed three times with ethanol, removed from the electrochemical cell, and dried

in a stream of nitrogen gas.

A preliminary electropolishing step, consisting of an electrochemical etch at a lower current density of 90 mA cm^{-2} for 30 s, was carried out each time before the above procedure to remove the top few nm of silicon from the wafer surface. This turned out to be necessary in this case because of the high doping level of the silicon original wafer, whose etching usually generates a

top crust of porous material with pores smaller than the rest of the film, presumably due to segregation of dopants at the surface of the wafer. The sacrificial layer was dissolved in a strongly basic solution (1 M aqueous NaOH), and the resulting silicon chip was first rinsed with copious quantities of a lesser acid solution (1:1:3 v/v HF:H₂O:EtOH), then with ethanol and finally dried with nitrogen gas. Such a procedure led to a particularly high degree of reproducibility of samples, which exhibit a uniform brown-orange color at the final stage (Figure 2-3).

2.1.3 The spectroscopic liquid infiltration method (SLIM)

Several techniques exist in order to determine the morphological features of PS, such as gravimetric measurements, scanning electron and probe microscopy, or nitrogen adsorption analysis at cryogenic temperatures (e.g., the BET, BJH, and BdB methods). Compared to these, the spectroscopic liquid infiltration method (SLIM) constitutes a faster and, above all, nondestructive alternative, and it was therefore adopted to check thickness L and porosity P of each freshly etched PS sample.

The SLIM is based on comparing data from two reflectance spectra: one obtained from the sample in air ($n_M = n_{air} = 1.000272$ at 20 °C) and the other from the sample immersed in a liquid of known refractive index (e.g. ethanol in this case, $n_M = n_{ethanol} = 1.3611$ at 20 °C). The overall apparatus to make these optical reflectance measurements is photographically pictured in the inset of Figure 2-9. A split optical fiber and lens set-up was used for both the illumination and the collection of the light reflected from the sample. The optical reflectance spectra of the PS film were acquired with a CCD-based spectrometer (Ocean Optics USB2000) attached to a bifurcated fiber optic cable. A tungsten halogen light source (Ocean Optics R-LS-1), providing a relatively broad effective wavelength range in the visible-near infrared (400-1000 nm), was used to illuminate the surface of the sample via one arm of the

bifurcated fiber. The light source was focused by a bi-convex lens onto the sample surface with a spot size of approximately 2 mm^2 , and the reflected light was channeled to the spectrometer through the same objective lens. Thus, both the spectral acquisition and light illumination were performed along the same axis, normal to the surface of the PS sample.

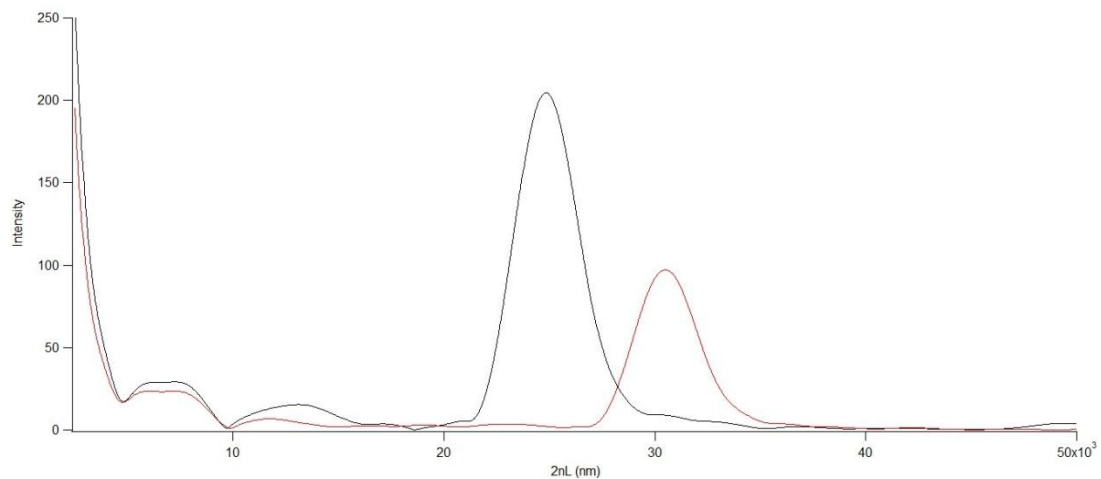


Figure 2-4 FFT peaks derived from reflectance spectra in air (black) and ethanol (red) of a PS film.

As a demonstrative example of how a SLIM analysis was usually performed, Figure 2-4 shows the FFTs of two reflectance spectra. The first is the one reported from Figure 1-3 and measured in air (black peak) while the second is the FFT of the reflectance spectrum measured from the same sample, but dipped in pure ethanol (red peak). As one can see, immersion of the sample in ethanol results, at the same time, in a redshift and attenuation of the peak. The position of the peak along the x -axis represents the EOT of the film into the medium (air or ethanol), assuming the pores within the light spot to have been completely wetted with ethanol. The EOT shifts from a value in air $EOT_{\text{air}} = 24848.2 \text{ nm}$ to a value $EOT_{\text{ethanol}} = 30508.9 \text{ nm}$ in ethanol. Since spectra were acquired immediately after etching the PS samples, the porous matrix is not oxidized and can be thought to be constituted by pure silicon.

Besides, considering the spectral region in which the FFT has been obtained (600-1000 nm), its refractive index is substantially not wavelength-dependent and can be, at the end, reasonably approximated to a value equal to $n_S = 3.8$. A numeric calculation which implements, therefore, a two-component (n_S and n_M) Bruggeman effective medium approximation theory gives, as a result, values of thickness and porosity equal to $L = 9808$ nm and $P = 72.2\%$ respectively, which are in this case pretty close to the desired ones.

Although the SLIM provides a local evaluation of L and P only in the area irradiated by the light spot (preferentially the center of the round PS chip) and it is not representative of the entire film, it has been the main characterization procedure also for samples in the subsequent fabrication steps, i.e. ozone oxidation and carbonization (see following section).

2.2 From porous silicon to carbonized porous silicon

All the PS samples presented in this work have been carbonized in the same way according to the receipt described in the following sections, which lightly differs from the original one developed by Kelly and coworkers in [57] (see subsection 1.4.3). In particular, great care has been paid in order to accurately control and vary the final content of carbon of CPS composites, also avoiding all the time- or human-dependent constraints which could affect somewhat their reproducibility.

2.2.1 The original carbonization procedure

As already mentioned in the introductory chapter, the carbon and CPS composites templated by Kelly and coworkers in PS rugate filters were proposed for the adsorption and detection of organic vapors. The process flow of Kelly's method is synthetically sketched in Figure 2-5:

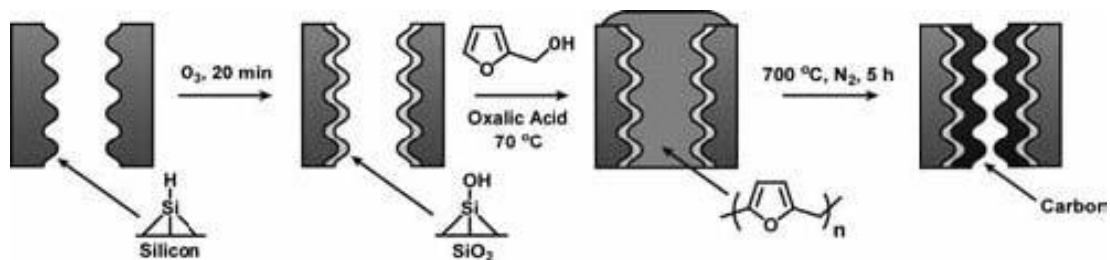


Figure 2-5 Kelly's carbonization chemistry process flow. Taken from reference [57].

Kelly's CPS composites were synthesized by thermal degradation of one of the more common polymers used as a precursor for amorphous carbon, i.e. the poly(furfuryl alcohol). Freshly etched PS rugate filter templates were first oxidized under a stream of ozone in order to provide strong adsorption sites for the furfuryl alcohol (FA) carbon precursor. Then, the remaining pore volume was filled with a solution of

dihydrate oxalic acid in FA, whose in situ polymerization yielded a resin-infiltrated film that was, at the end, carbonized at 700 °C for 5 h. These CPS composite materials have shown to still retain some porosity, in spite of a reduction in the average pore diameter. While the aim of such a former work was to achieve an as much large amount of carbon as possible within the pores of the rugate filter vapor sensors, the main requirement of the present one was rather to reach a compromise between the final carbon content of the samples and their optical transduction capabilities. Indeed, being carbon a strong light absorber, an excessive quantity of carbon might lead to the complete depletion of Fabry-Pérot interference fringes in a ~10 µm thick PS optical film immersed in liquid. For this reason, here the FA had been diluted in a solvent, i.e. ethanol, providing different kinds of samples with different percentages of carbon (see next chapter), depending on the initial concentration of the neat precursor.

2.2.2 Ozone oxidation and furfuryl alcohol infiltration

The FA polymerization is acid-catalyzed. As confirmed by Fourier-transform infrared spectroscopy analysis [10], an oxidative treatment on PS with ozone can provide a silicon oxide surface with a high percentage of terminal silanol functionality (Figure 2-5). Ozone oxidation gives quite hydrophilic PS surfaces and forms oxides more hydrated than in thermal oxidation procedures. In the original carbonization receipt, oxalic acid (in concentration equal to 5 mg mL⁻¹) was added to the FA precursor to improve the chemical kinetics of the subsequent polymerization. Anyway, the surface protons within a just ozone-oxidized PS sample have been found to be sufficiently acidic to catalyze, on your own, the reaction. Therefore, the present-work samples were simply oxidized in a flow of ozone gas (with a flow rate of 1.5 SCFH), at room temperature, for a period of 20 min. After checking thickness

and porosity with the SLIM, the resulting red-colored oxidized PS chips (Figure 2-6) were blocked on the chuck of a spin-coating system, programmed to run a two-steps rotation. 100 μL of neat or diluted FA were gently spilled on the surface of the samples, which were initially spun at a frequency of 300 rpm for 1 min, then at 3000 rpm for two min. The former slower rotation step was intended to favor the infiltration of the carbon precursor into the nanopores of the film, while the faster one to mechanically dry the excess amount of FA, avoiding the formation of aggregates on top of sample surfaces.

Samples prepared in this way look very uniform and without patches of alcohol residue, even by spinning neat FA. Anyway, the final CPS composites did not display Fabry-Pérot fringes unless the percentage of FA relative to the total

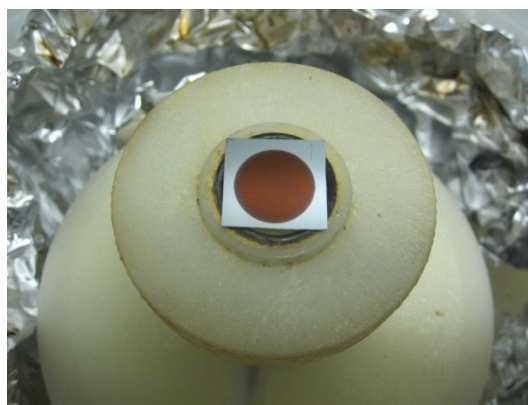


Figure 2-6 Ozone oxidized PS sample before FA infiltration.

volume of solution was below a threshold value of 25% (1:3 v/v FA:EtOH).

2.2.3 Thermal polymerization and carbonization

Immediately after being spun, the FA-impregnated PS samples were put into a covered ceramic container and loaded inside the chamber of a box oven (Thermo Scientific Thermolyne FD1535M, right portion of Figure 2-7) set to reach a target temperature of 70 $^{\circ}\text{C}$ with a ramp rate of 10 $^{\circ}\text{C}/\text{min}$. Thus, they were left there for 16 h (the time starting as soon as the target temperature was reached) in an indoor air atmosphere. During this period, the FA undergoes an acid-catalyzed thermal polymerization process, yielding poly(FA) infiltrated PS films.



Figure 2-7 Box oven and tube furnace utilized for the polymerization and carbonization steps, respectively. The inset shows some CPS composite chips at the final stage.

Once the 16 hour time was elapsed, samples were removed from the box furnace, placed on a ceramic crucible and introduced in a tube furnace (Thermo Scientific Lindberg Blue M, left down corner of Figure 2-7) sealed up with a corked tube. In order to purge the furnace of oxygen, nitrogen gas was flowed for 30 min at a rate of 1 SLPM and at a temperature of 50 °C (10 °C/min). Afterwards, under the same nitrogen flow, the temperature was again increased at a rate of 10 °C/min up to 700 °C, and the poly(FA)-PS composites carbonized at this temperature for 55 min. Finally, the furnace was set to cool to room temperature at a ramp rate of 5 °C/min and the samples removed at 200 °C to avoid cracking due to thermal shocks. The inset of Figure 2-7 shows how the dark CPS chips appear after the entire preparation was completed. As it will be better highlighted in the next chapter, the extent of the carbon layer thickness synthesized within the CPS optical chips was simply estimated by considering the final FFT interferometric peak intensities displayed by samples. Unlike more specific quantitative or carbon-based typical analysis, as energy-dispersive X-ray or Raman spectroscopies, this fast characterization does not

provide any information about the carbon form produced, but it was performed on all the fabricated samples and allows rapid comparisons.

It has to be underlined that the just described carbonization procedure has been nearly optimized in order to better control the final carbon content inside CPS composites, not to improve the performances of the ultimate device or the economy of the process. For instance, a mild oxidation for few minutes at low temperature, like the one carried out using ozone as oxidant, tends to produce electrical insulating oxides, in principle not suitable for electric-field-assisted experiments. Anyway, the oxide layers forming in these conditions were probably very thin since they seem to have not affected the electroadsorption/desorption measurements. Besides, the ozone oxidation usually improves mechanical stability in PS, and the control of the carbon content is easier by harnessing only the acid groups deriving from the ozone oxidation as catalyzing agents. Even if the use of oxalic acid can substitute or be associated to the ozone oxidative step, the presence of this compound in the FA precursor could trigger an uncontrolled polymerization even at room temperature, leading also to limitations in samples reproducibility. Still concerning the FA polymerization, despite some indications suggesting the 70 °C thermal process does not need such a long incubation period of 16 hours, this step has been maintained since it takes place in air atmosphere, it is not gas-consuming and can be easily performed overnight. By contrast, the nitrogen flow related to the 700 °C pyrolysis procedure is the most critical parameter of the entire process in order to control as fine as possible the carbon coating layer thicknesses. The carbonization period has been drastically reduced from 5 hours to less than one not since this time turned out to be largely sufficient to produce good optical (and stable) CPS chips, as well as it is gas-saving and more verifiable. In this case, the more important origins of error in

reproducibility can stem from a wrong sample positioning inside the furnace (causing undesired temperature gradients if it is far from the tube furnace center) or oxygen contaminations, which can lead to too much carbonaceous materials or, in the worst case, even to the complete combustion of the sample.

Despite some ad hoc tests had been performed to compare pros and cons and feasibility of modified carbonization techniques, the results are not definitive and go beyond the scope of the present thesis.

2.3 Porous silicon/carbon coupled opto-electrochemical sensors

The CPS composite chips were mounted inside a custom-designed flow cell (Figure 2-8) joined with a peristaltic pump (inset of Figure 2-9) to allow circulation of

analyte-containing or free liquid media in a closed loop.

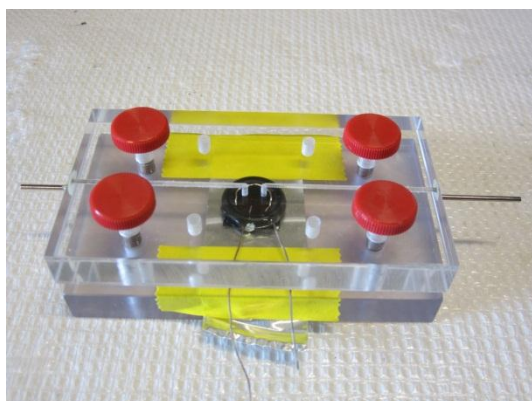


Figure 2-8 Opto-electrochemical flow cell.

The total volume of liquid employed in all the experiments was equal to 5 mL and it was mechanically agitated at a flow

rate of about 1 mL min^{-1} . The flow cell was optically transparent to facilitate

acquisition of reflectance spectra by the same instrumentation used for the SLIM determinations previously described (see subsection 2.1.3). The chip was contacted on the backside with a strip of aluminum foil, enabling its use as working electrode. Instead, a customized platinum counter electrode had been expressly designed to be fitted inside the flow cell rig and circularly shaped to improve electric field uniformity. In order to avoid leakages, the platinum loop was directly drawn inside the inner portion of a circular O-ring, also provided by a homemade reference electrode (a silver chloride wire) allowing measurements in a three-electrode configuration, as well as in a two-electrode one. Nevertheless, in the present thesis, only two-electrode measurements will be presented, in order to facilitate comparisons. Therefore, the electrodes were connected to a general purpose electrochemical potentiostat/galvanostat (Pine Instrument Company AFCBP1) set to

work in potentiostatic conditions. The current analog output was transferred from the bipotentiostat to a computer-controlled analog-to-digital card by a programmable current/voltage source (Keithley 2601 Sourcemeter), interfaced with a customized LabVIEW program expressly written to collect the values of the current flowing between the CPS working electrode and the platinum counter electrode as a function of time.

The overall combined optical/electrical measurement system that has been assembled for the time-resolved tests is showed in Figure 2-9. Electrical data were collected at a ratio of 10 acquisitions per s. On the other hand, unless noted otherwise, optical data were typically acquired every 10 s by the CCD spectrometer software (Ocean Optics OOIBase32) and preliminary processed and monitored by a purpose-written program macro (Wavemetrics IGOR Pro). Optical and electrical parameters (timescales, applied bias, sweep rates) as well as sensing ones (pH, ionic strengths, buffer solutions, biomolecular complexes, concentrations) will be specified in the next chapter for each proposed experiment.

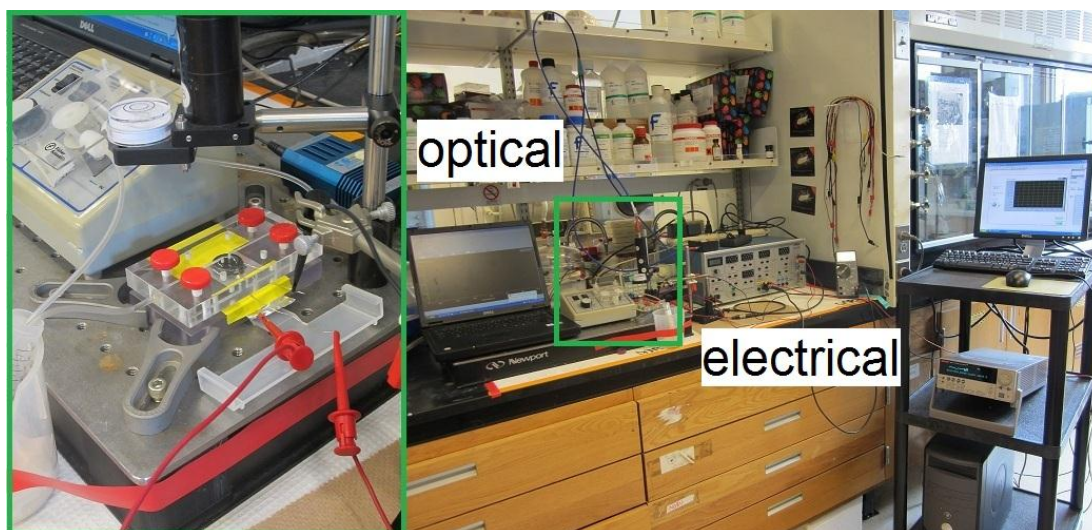


Figure 2-9 Overview of the whole instrumentation system. The inset zooms on the combined opto-electrochemical device.

3 Experimental results

The present chapter reports some test experiments accomplished with the new described opto-electrochemical combined sensors, aimed to demonstrate their usefulness both in sensing than in energy harvesting applications.

In as much as sensing fields are concerned, the admission into and diffusion through nanoscale pores by molecules is a fundamental process of great importance, for instance, to bioanalytics and separations science. The constricted environment in a nanopore has a substantial influence on molecular transport that can be harnessed for filtration [58-59], controlled release, nanofluidic [60] or gating applications [61-62]. Artificial systems with abiotic micro- or nanometer sized pores (e.g., polymeric, inorganic, and composite membranes) designed to take advantage from such processes are usually more stable and predictable compared to biological pores [63]. Among these, PS offer a versatile synthetic alternative to control analyte transport and binding: (i) the high surface area of the 3D material allows to capture and concentrate significant quantities of target molecules, (ii) the porous nanostructure can be tuned during synthesis to yield a range of pore sizes, and (iii) optical structures can be incorporated into the film to provide sensitive, label-free quantification of analyte binding. The drive to decrease sample volumes and increase throughput has led to microanalysis PS-based chips that combine these components within a volume of a few cubic micrometers. In addition, conventional analytical techniques like chromatography or electrophoresis tend to remove the separation process from the detection event, both spatially than temporally. PS Fabry-Pérot optical films provide, in this case, a means to detect and identify molecules

simultaneously with, and in the same ultrasmall physical location as, the separation event, thus improving sensing fidelity in complex media.

The size-selective filtration and separation abilities of PS have been demonstrated for a wide range of molecular species [64-65]. In a former work [66], by exploiting the native negative charge of thermally oxidized PS optical chips, Chen and coworkers succeeded to admit or exclude (from nanophase pores) different kinds of proteins based on their size and charge. Each biomolecule displays a surface charge distribution depending on factors as its chemical configuration or pH and ionic strength of solutions biomolecular complexes are dissolved in. As formerly showed, capture/release events and transport of electrically charged proteins can be even better controlled if assisted by an electric field applied to a conductive Salonen- or Chen-like material, yielding to a very powerful support to identify biomolecules based on their size, charge, and diffusional characteristics. Nevertheless, Chen's electroadsorption/desorption results do not provide any information about the current behavior of the device along with the optical sensing. A parallel electrical assay can be used not only to monitor the evolution of a PS matrix in different ionic liquids upon voltage application, but also work as an additional transduction method in case one of the two, for whichever reason, failed.

3.1 Tuning the carbon content and preliminary stability tests

The two main prerequisites expected from a conventional working electrode are stability in electrolytic solutions and conductivity. A carbon film upholstering the pore walls of a PS-based electrode and synthesized through the Kelly's carbonization chemistry can meet both of these two requirements.

The final carbon amount lining the present-work CPS composites depends on the initial quantity of the FA carbon precursor casted on top of the PS surface. For a CPS sample to display Fabry-Pérot fringes, the FA had not been used neat but it was diluted in ethanol. According to the carbonization procedure described in the previous chapter, CPS layers did not display any interferometric optical pattern if the relative percentage of FA respect to the 100 μ L total volume solution was higher than a threshold value, approximately estimated to be around 25%. Therefore, in the present thesis, the FA percent range investigated to produce CPS optical chips had been limited in a window comprised between 1% and 25%. Figure 3-1 shows several FFT interferometric peaks, each one corresponding to a CPS film characterized by the carbon precursor percentage marked by color.

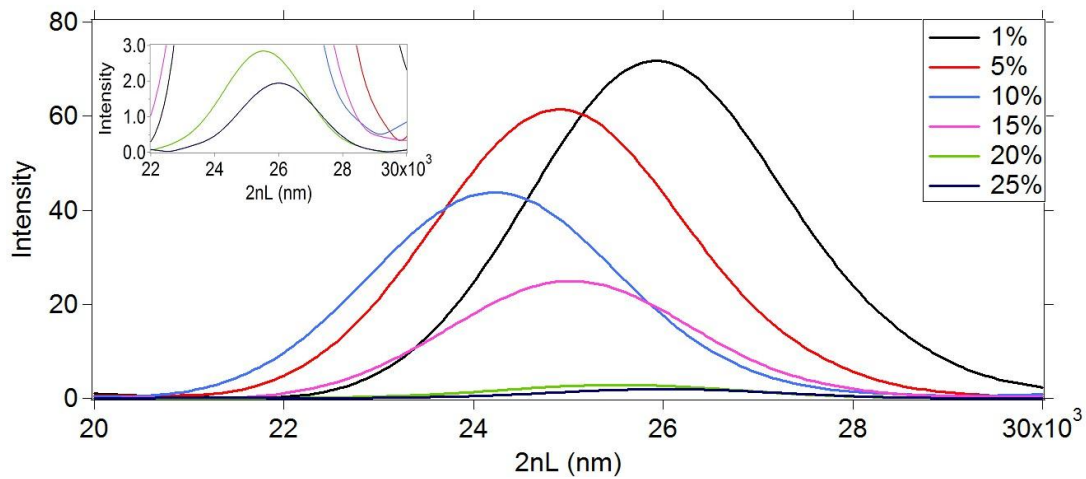


Figure 3-1 FFT peaks in air of CPS films containing a different percentage of carbon. The inset is the magnification corresponding at the higher concentrations: 20% (green line) and 25% (dark blue line), respectively.

The peaks of Figure 3-1 are FFTs from CPS reflectance spectra all collected in air. In this case, the shift in the EOT (2nL) between one peak and another is due to inequalities in the physical thickness L of the original PS samples. Increasing the FA quantity into the reaction solution means to increase the carbon amount will be present on the CPS composite, and thus the light absorption capabilities of the final sensor. The higher the carbon content is, the lower is the amplitude of the Fabry-Pérot interferometric fringes, and so the intensity of the corresponding FFT peak. Even a very small percentage (e.g., 1%) of carbon precursor leads to pretty dark samples and to a significant depletion of the FFT intensity. By augmenting the carbon content, a monotonic decrease of the FFT peak intensities is observed until the higher percentages are reached. In these cases, as from the inset of Figure 3-1 showing the magnification of the 20% and 25% FFTs, the intensities were very low but peaks could still be used for interferometric sensing.

In the two previous chapters, it has been widely stressed that water is a huge corrosive agent for freshly etched or oxidized PS, and that a carbon layer can protect

PS surfaces from hydrolytic attack. Chen's samples, hydrocarbonized according to the Salonen's method, demonstrated a pretty good stability in aqueous buffers, as well as upon application of different voltages. Nevertheless, as formerly mentioned, they were not stable in case of positive potential. For this reason, the stability of the new Kelly's composites has been tried out under positive bias, continuously applied between the working and the counter electrodes, with samples always immersed in reference deionized water (pH = 5.3 at 23.2 °C). Figure 3-2 shows the optical method that has been used in this case to check stability of the present-work sensors, consisting in monitoring the percent changes in the EOT as a function of time.

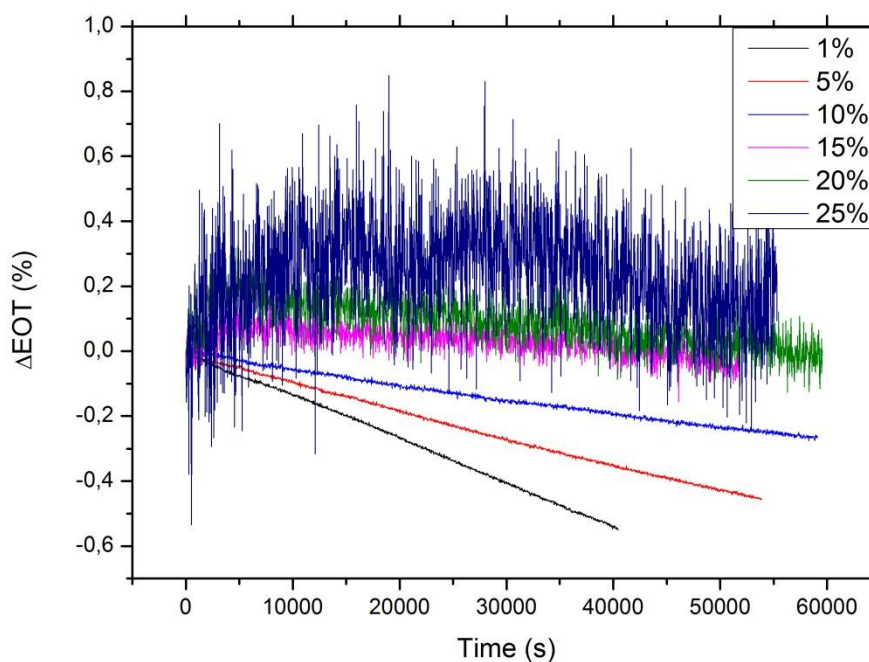


Figure 3-2 Changes in EOT of CPS optical films as a function of time. A constant +1 V potential was applied in water to the different carbon-containing CPS electrodes.

After 30 min samples were immersed in liquid, +1 V was applied to the CPS electrode and optical data acquired, in this case, every 30 s. Due to the very long timescales and the optical nature of such a stability test, a voltage lower than the

water electrolysis potential difference (1.23 V) was chosen in order to avoid water splitting effects. Samples and carbon percentages from Figure 3-2 are the same of Figure 3-1. All the CPS films displayed remarkable endurance under these rather extreme stress conditions. In order to make adequate comparisons, two factors have to be taken into account when considering the % Δ EOT variations: the blueshift decrease (indicating a dissolution of the PS matrix), and their amplitudes (related to the final sensitivity of the sensor). Of course, samples with minor quantities of carbon undergo faster degradation, whose rate is proportional to the carbon content. By contrast, increasing the carbon amount leads to almost completely stable samples, but at the expense of the optical signal quality. Anyway, even a 1% CPS sample can withstand up to more than eleven hours in these conditions, by showing an overall blue shift of less than 0.5%.

Table 3-1 Linear fit parameters resulting from linear interpolation of data from Figure 3-2.

<i>Carbon %</i>	<i>Slope (10^{-6})</i>	<i>Standard Error (10^{-8})</i>	<i>RSS</i>	<i>Pearson's r</i>	<i>Adjusted R^2</i>
1	-13.394	1.11428	0.02912	-0.99955	0.99909
5	-8.44459	0.975442	0.07002	-0.99884	0.99768
10	-4.47958	0.886472	0.08391	-0.99628	0.99256
15	-1.76583	5.91607	2.19887	-0.58924	0.34682
20	-2.97173	7.26562	5.79716	-0.68179	0.46456
25	-0.948481	25.3606	52.5894	-0.0881	0.00721

As it appears well-rendered by the CPS composites with the lowest carbon percentages (1%, 5% and 10%), the slow dissolution of a CPS matrix has, in these conditions, a linear trend. Table 3-1 reports results from linear regression valuations computed for all the five carbon percentages. A more strict statistical calculation

could directly connect the parameters of Table 3-1 to the standard deviation from an EOT average value, and thus to the final sensitivity of each CPS optical film. Nevertheless, the optical signal noise can be easily quantified by just looking at the equilibrium (no voltage applied) measurements, and here it is only pointed out the main reason for which different kind of samples, from almost opaque to semi-transparent, have been produced. Notwithstanding a minor stability compared to higher percentages of carbon, a 1% CPS optical film shows, both in equilibrium than not-equilibrium steady states, very low changes in the $\% \Delta \text{EOT}$ (of the order of 0.005%), and so it may have a sensitivity of few nm as far as variations in the EOT are concerned. Moreover, the tunable voltage window achievable by an electroadsorption-based analyte capture method can potentially allow detection, as well as transport, of extremely small quantities of electrically charged analytes or ionic species in solution.

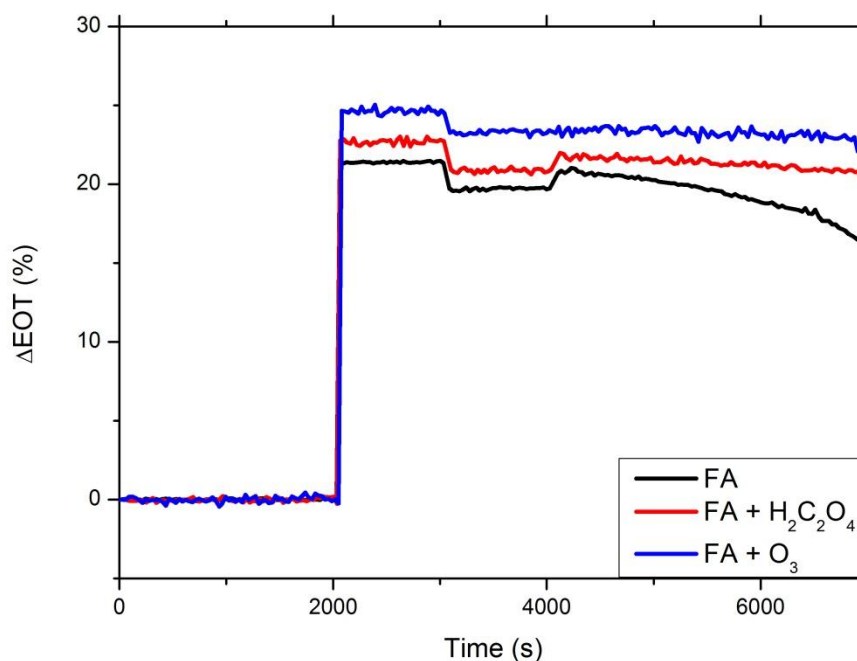


Figure 3-3 Changes in EOT as a function of time of differently prepared 10% CPS optical films upon immersion in test liquids.

Finally, some quick stability tests performed in various (stationary) liquids are presented in Figure 3-3. The samples were three same percentage (10%) CPS composites, synthesized by using a different catalysis strategy for the polymerization process: (i) ozone (blue line), (ii) 5 mg mL⁻¹ oxalic acid (red line) and (iii) neither ozone nor oxalic acid (black line). Optical reflectance spectra were collected first in air to establish a common initial horizontal baseline in the % Δ EOT value. Afterwards, ethanol was poured on top of the samples surfaces in order to wet their pores walls, this resulting into a swift redshift of the EOT at time $t = 2000$. After a new steady value was reached, ethanol was substituted with deionized water and then with sodium hydroxide at pH = 13, a very basic solution generally used to dissolve PS films. The noisy behavior corresponding to a CPS sample prepared both with ozone than oxalic acid is not displayed in Figure 3-3 for clarity reasons. The composites were prepared in the same way according to the procedure described in the previous chapter, including the 70 °C polymerization period 16 h long. The only film that undergoes significant degradation over this timescale is the one for which any catalyzing agent has been used to polymerize the FA. By comparison, the other two show a longer stamina to nucleophilic attack by NaOH hydroxide ions (OH⁻), even if they will, anyhow, start to dissolve after a short while, most likely because of the pretty low carbon content. The choice of ozone over oxalic acid was preferred, as previously explained, to better control reproducibility of samples.

3.2 Electrochemical measurements of double-layer capacitances

Information about capacitance of an electrochemical system can be gained by applying an electrical perturbation to it and observing the resulting changes in its current vs time characteristic.

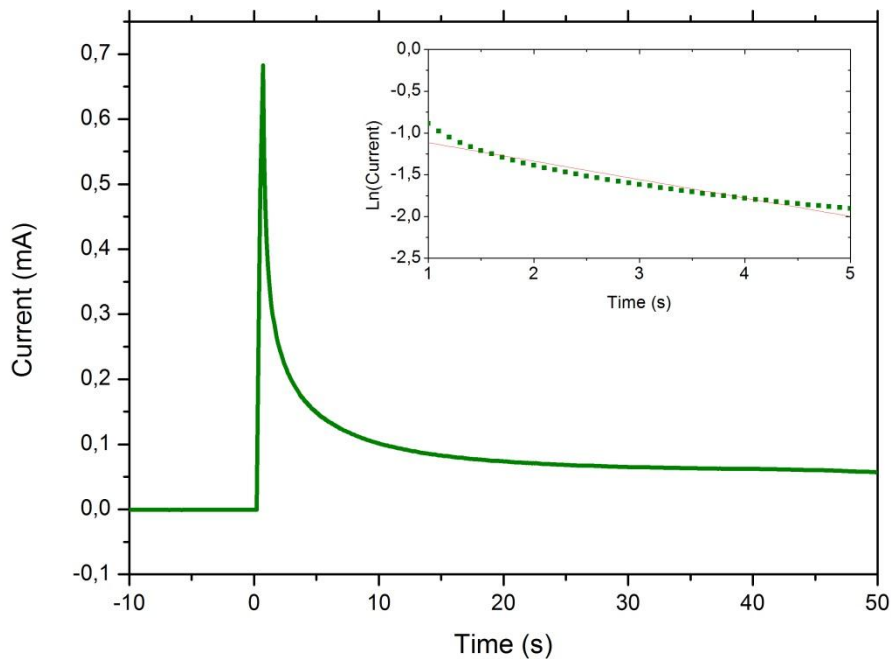


Figure 3-4 Current transient resulting from a -0.5 V potential step on a 20% CPS sample. The inset shows the corresponding natural logarithm of the current vs time trace.

The capacitance of a CPS composite is defined by the electrical double-layer in the electrolytic solution. A two-electrode cell can be approximated by an electrical circuit with a resistor, R_s , representing the solution resistance and a capacitor, C_d , representing the double layer at the CPS/electrolyte interface. Since C_d is generally potential dependent, the proposed model in terms of circuit elements is strictly

accurate only for experiments where the overall cell potential does not change very much. Hence, C_d can be determined through the familiar RC equation:

$$\tau = R_S C_d$$

where τ represents the exponential decay constant of the electrode, i.e. the time at which the current for charging the double-layer capacitance drops to 37% of its initial value.

Interfacial capacitances (C_d) and charging currents (I) of CPS devices have been measured in the same conditions as Chen's ones, according to the procedure described in [20], by application of a -0.5 V non-Faradaic potential step to the CPS film. The typical corresponding behavior of the exponentially decaying current is reported, by way of example, in Figure 3-4, in the case of a 20% CPS sample. The electrolyte was constituted by a PBS buffer at an ionic strength of 0.0075 M. At a time $t = 0$, a bias (ΔV) of -0.5 V relative to the platinum counter electrode was applied and maintained for 50 s. Thus, the natural logarithm of the current I (inset of Figure 3-4) was interpolated by a linear fit, whose slope ($-1/\tau$) was used to calculate the time constant τ , while R_S was obtained through the Ohm's law (V/I). Based on three replicate -0.5 V steps, τ and R_S average values were calculated, the measurements then repeated for three different representative carbon percentages: 1%, 10% and 20%. The results computed for C_d (not normalized) are summarized in Table 3-2.

Table 3-2 Values of τ , R_S , and C_d obtained from different carbon-containing CPS composites.

	τ (s)	R_S (k Ω)	C_d (μ F)
1%			
1	0.173782782	239.3489708	0.726064463
2	0.178271233	243.0724356	0.733407851

3	0.174013517	245.2182442	0.709627124
Avg	0.175355844	242.5222312	0.723050597
10%			
1	0.320277745	69.8031551	4.588298973
2	0.303616375	71.33685262	4.25609434
3	0.281565617	71.18451025	3.955433794
Avg	0.301819912	70.76806945	4.264916574
20%			
1	1.257924927	8.786110916	143.1719835
2	1.294196821	8.778089888	147.4349019
3	1.123418788	9.097194425	123.4906869
Avg	1.225180179	8.884676894	137.8981131

By considering an overall area of $\sim 1.2 \text{ cm}^2$, the final values of C_d for 1%, 10% and 20% CPS composites were found to be equal to (0.603 ± 0.001) , (3.55 ± 0.26) and $(115 \pm 10) \mu\text{F cm}^{-2}$, respectively. The values are visualized in the graph of Figure 3-5 as a function of the carbon content percentage.

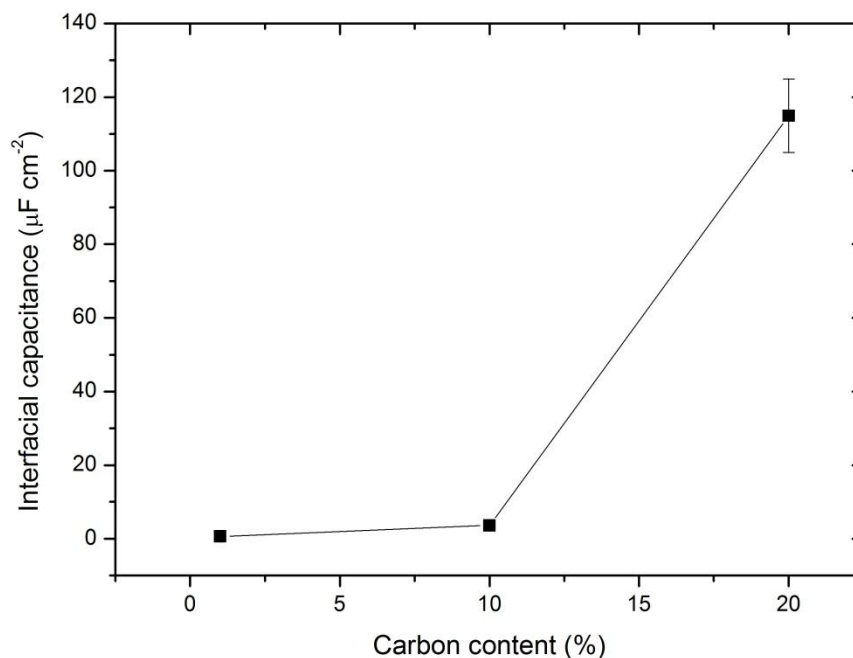


Figure 3-5 Dependence of the interfacial capacitance of CPS composites on the carbon content.

The obtained values are of the same order of magnitude of Chen's device, whose interfacial capacitance C_d was measured to be $\sim 8 \mu\text{F cm}^{-2}$ ($\tau = 0.4 \text{ s}$, $R_S = 50 \text{ k}\Omega$). However, the ease in increasing the FA precursor achievable by the present carbonization method suggests, as somewhat foreseeable, a not linear dependence between carbon content and capacitance, which can be rapidly enlarged as it is shown in Figure 3-5. Anyhow, the results can furnish additional clear evidences about reliability of the carbon tuning process and, as a consequence, on the reproducibility of the CPS fabrication method.

3.3 Coupled opto-electrochemical biosensing

Ionic strength and pH are two important parameters as far as electric-field-assisted biosensing experiments are concerned. The buffer ionic strength window explored by Chen and coworkers in [20] ranged from 0.001 to 0.15 M. Only buffer solutions (pH 6.7) with ionic strength of 0.007 M, anyway, were used in all the experiments addressed to quantify protein loading and concentration efficiency as a function of applied bias and bulk solution concentration. Therefore, for all the measurements presented in the current section as well, an equivalent ionic strength value was chosen (7.5 mM), and obtained by mixing the PBS (Invitrogen) buffer with ultrapure deionized water (final pH = 7.5 at 22.9 °C).

As such as medium-low ionic strength value is preferred, in this case, in order to lower the sensor optical response stemming from the ionic salts present into the buffers, trying at the same time to do not denature or otherwise deactivate the biomolecule of interest. Buffered solutions are indeed necessary to keep the correct pH for many biomolecular complexes to work, as enzymes. If the pH moves outside of a very precise narrow window, for instance, the enzymes can undergo significant denaturation which can be even permanently disable their catalytic activity. On the other hand, buffers as PBS contain a number of inorganic salts (such as KH_2PO_4 , NaCl , Na_2HPO_4) that, once dissolved in water, form electrically charged species which may interfere with the optical based interferometric detection of electroadsorbed/desorbed molecules that is harnessed by the CPS sensors. For this reason, a check in pure buffer turns out to be strictly necessary in these kinds of measurements, especially when a lot of different parameters are involved.

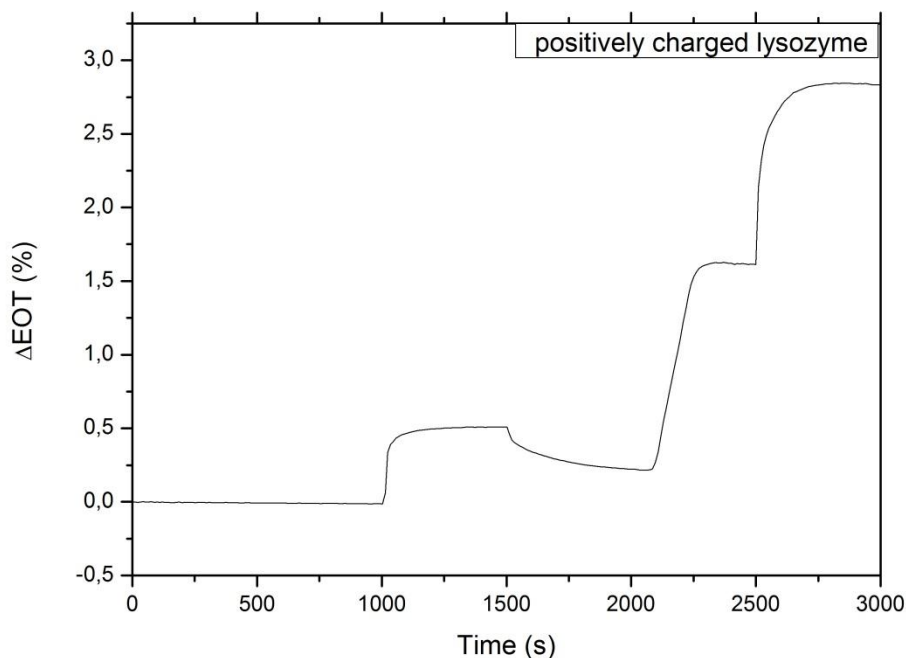


Figure 3-6 Optical response of a 10% CPS sensor upon electric-field-assisted test with positively charged lysozyme.

Chicken lysozyme (molecular weight ≈ 14.3 kDa, isoelectric point \approx pH 11) was selected also for these studies as a test protein, and used as-received (Sigma-Aldrich) without further purification. At pH = 7.5, lysozyme exhibits a net positive charge and can be therefore attracted by applying a negative potential to a CPS film. The Figure 3-6 illustrates the generally adopted procedure for the detection of electroadsorbed enzyme, by using a 10% CPS optical sensor. An initial horizontal baseline was established in pure buffer solution holding the film at 0 V. A negative bias (-2.75 V) was then applied just in PBS (1000 s) and maintained for about 8 min. Afterwards, the voltage was set back to 0 V until a new equilibrium was reached (2000 s). Hence, a solution containing lysozyme, at a concentration of 10 mg mL^{-1} and dissolved in the identical buffer, was introduced into the flow cell system (2000 s) with the film still held at 0 V. As soon as a new steady state was established, the same negative

bias of the control test was applied (2500 s) and kept from the same period (500 s). The $\% \Delta EOT$ profile of Figure 3-6 shows three different sharp redshifts: the first (at ~ 1000 s) is ascribable, in first approximation, to cationic Na^+ atoms still present into the control buffer; the second (~ 2000 s) is relative to lysozyme infiltrating the CPS matrix for normal diffusion; the third (~ 2500 s), instead, is consistent with a voltage-dependent electroadsorption phenomenon driving protein into the pores. In this case, the greater contribution to the optical signal given by lysozyme respect to ionic species can be roughly estimated by looking at the differences between the baselines values of Figure 3-6. However, such an evaluation is oftentimes not so easy, since many are the parameters which can affect the final result, such as the magnitude and sign of the charge on the ions, biomolecules and applied bias. In particular, unlike Chen's composites, where the ionic strength of the electrolyte was found to exert only a minor effect, the optical response of the present-work sensors turned out to be, as showed in Figure 3-6, strongly influenced by ions. Anyway, a parallel electrical assay can help to better understanding these phenomena. Apart from providing an additional check for those measurements lacking of such a clear evidence, it can also be used to test the electrochemical performances of the device.

3.3.1 Positively charged biomolecules

Lysozyme is a relatively small globular protein with dimensions of 3.0 nm X 3.0 nm X 4.5 nm and an isoelectric point of pH 11.1, which exhibits a net positive charge if dissolved in a buffer below this pH. Therefore, it is a very good candidate to test the opto-electrochemical behavior of a CPS sensor under different conditions. Figure 3-7 displays an experiment, equivalent to the one presented above, in the case of a 1% CPS coupled device, for which both the optical (a) than electrical (b) characteristics are provided.

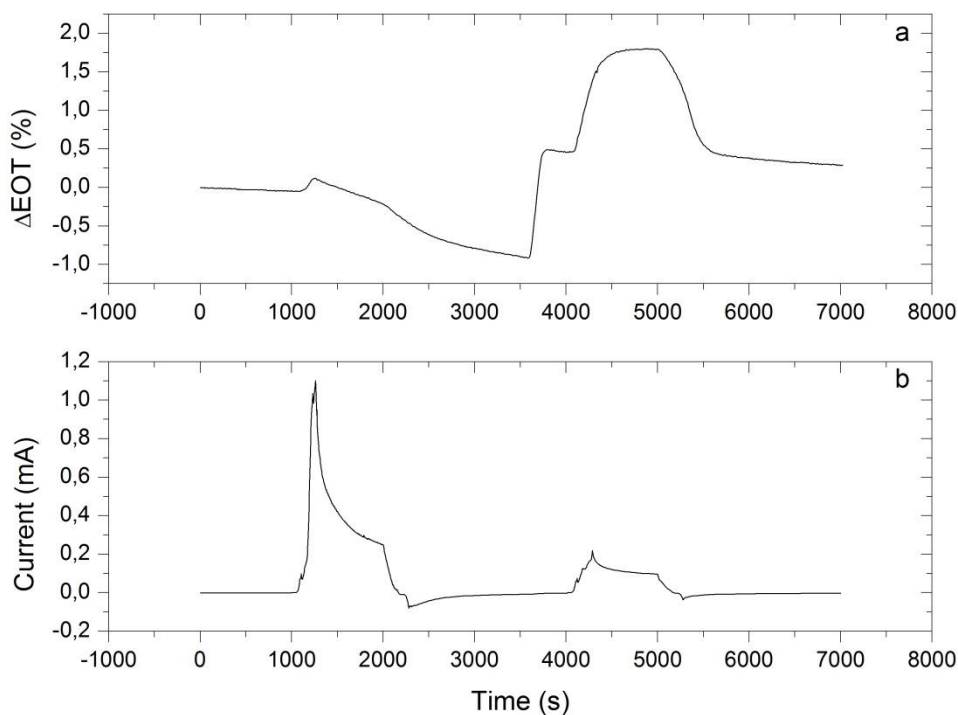


Figure 3-7 Optical (a) and electrical (b) responses of a 1% CPS sensor upon electric-field-assisted test with positively charged lysozyme.

At the beginning, in order to establish common horizontal baselines, optical and electrical data were still collected in pure buffer at 0 V, in this case from time t_0 (0 s) to time t_1 (1000 s). An high negative bias (-2.75 V) was applied at time t_1 , maintained until time t_2 (2000 s), after which it was set back to 0 V. Lysozyme was introduced at time t_3 (3500 s) and the voltage applied again between time t_4 (4000 s) and t_5 (5000 s). Finally, at time t_5 , the film was held back to 0 V for the rest of the experiment. As it is deducible from graphs of Figure 3-7, the overall response of the opto-electrochemical sensor is asymmetric. In so far as the % Δ EOT changes are concerned, the application of such a high negative bias in PBS only (t_1) leads, at first, to a feeble redshift. In a short while, anyway, the film starts to degrade by showing a quite pronounced blueshift (most likely due to the combination of the high applied bias and the very low carbon content inside the CPS sample), which is just alleviated

by setting the bias back to 0 V (t_2). Introduction of lysozyme (t_3) results in an instantaneous increase in the value of % Δ EOT as long as protein infiltrated the porous matrix. After equilibrium, a large redshift is observed upon repeating application of the negative bias (t_4). The % Δ EOT profile reaches a saturation value around the time at which the electrode was held back to 0 V (t_5). After that, a blueshift takes place, as steep as the prior redshift but more abrupt of the one observed in PBS. Despite these results are similar to those presented in the previous experiment (Figure 3-6), it is not as simple, in this case, to determine the quantity of electroadsorbed lysozyme. Although the % Δ EOT variation first increases (t_4) and then returns (t_5) to the value established by the previous baseline at 0V, suggesting that biomolecules were successfully captured into the CPS matrix and then released back into the bulk solution, it is hard to discriminate between the contributions coming from protein rather than ions to the redshift observed at time t_4 , due to the large blueshift taking place between time t_1 and t_3 . On the other hand, by looking at the current characteristic (Figure 3-7-b), the electrical response of the sensor with respect to ions (t_1) and ions plus lysozyme (t_4) is specular to the optical one. In this case, charging effects, akin to those formerly showed (Figure 3-4), are observed both in PBS than in the presence of lysozyme. By comparing the two graphs of Figure 3-7, it can be gathered that sample degradation in pure buffer ultimately depends on high charging currents involving the CPS/electrolyte interface. These effects are high in PBS, but can be attenuated in the presence of lysozyme infiltrated into the film, thus leading to an even more stable material. Summarizing, the combined methods are both sensitive to low quantities of ionic species and electrically charged biomolecules into aqueous solutions, the optical displaying a higher response to biomolecules and a lower one to ions, and vice-versa the electrical. In principle, such

a coupled technique can be used to specify how much of the biosensor optical response derives from biomolecules and how much from ions. Otherwise, it provides a means to characterize biomolecules based on their electrical transport features. Anyway, the system is here presented just as a proof of concept and tried out under different stress conditions.

Time-resolved results as the ones from Figure 3-7 were obtained by synchronizing the electrical with the optical response of the sensor. In order to appreciate tiny redshifts like the one observed at time t_1 , it was not applied a spike potential but bias was gradually decreased from 0 down to -2.75 V (t_1 and t_4) and back (t_2 and t_5) at a pretty low rate (10 mV s^{-1}). Indeed, occurring into a dynamic liquid environment, the optical signal needs more time respect to the electrical one to stabilize into an averaged value. As a consequence, optical data are somewhat delayed compared to the current measurements. Performances and resolution of the device have been thus tested again with positively charged lysozyme by varying the applied voltage rate, i.e. exploring its behavior at low (10 mV s^{-1}), medium (25 mV s^{-1}) and high (50 mV s^{-1}) values. The outcome of this trial is reported in the graphs of Figure 3-8, in the case of a 10% CPS sensor.

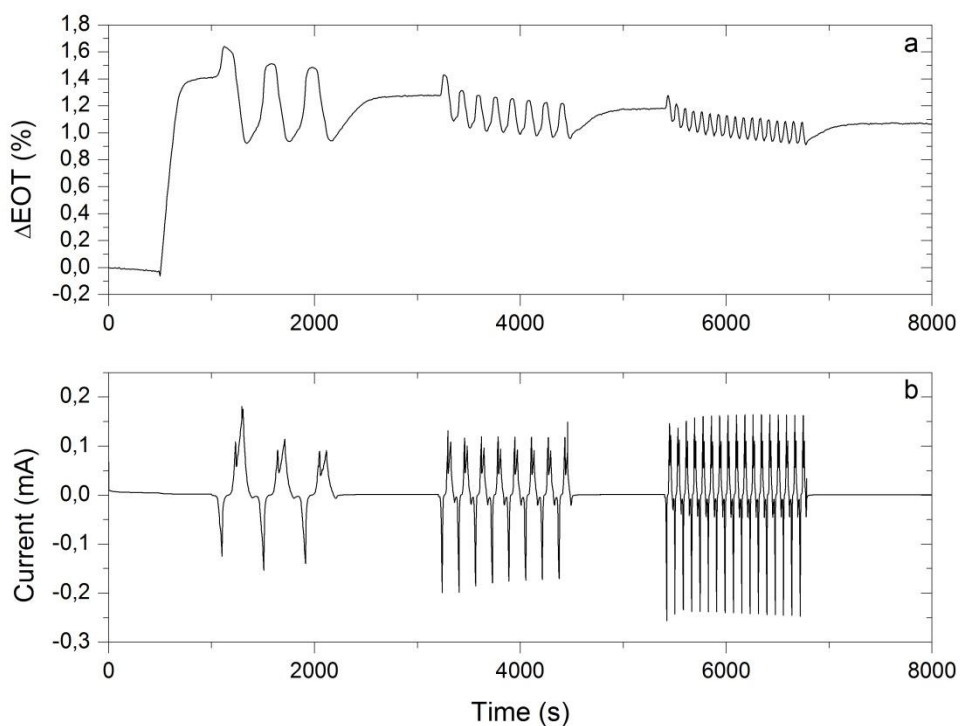


Figure 3-8 Optical (a) and electrical (b) responses of a 10% CPS sensor upon electric-field-assisted test with positively charged lysozyme, varying the potential between -1 V and +1 V.

This case, lysozyme was introduced at time $t = 500$ s, still resulting into an abrupt increase of the $\% \Delta EOT$. Initially, the potential was swept between -1 V and +1 V at the lowest rate for three times (as a guide to the eye, at ~ 2000 s). After an equilibrium period (during which the film was always held at 0 V), bias was again applied in the same window (-1 V, +1 V) but increasing the rate and number of repeats as well. Figure 3-8 shows a good correspondence between optical and electrical measurements in this range. Despite the investigated bias frequency values were very low (2.5 mHz, 6.25 mHz and 12.5 mHz, respectively), the $\% \Delta EOT$ profile displays a periodic modulation which is directly linked to the current measurements. As in the preceding experiments (Figures 3-6 and 3-7), to a negative bias corresponds a redshift in the optical thickness (the current values of Figure 3-8-b are reported, in this case, inverted respect to those of Figure 3-7-b). By progressively

passing from -1 V to +1 V, the current flow changes direction and a blueshift occurs as long as bias come back to 0 V and, then, to -1 V again. In so far as the first (out of three) voltage ramp at 2.5 mHz is concerned, such blueshift has probably two different causes: the former can be seen as electrostatic repulsion between positively charged lysozyme and CPS surface upon application of a positive voltage, which implies that infiltrated proteins are repelled from the porous layer; whilst the latter involves a degradation of the film rather under positive than negative bias conditions. Anyway, the other two voltage ramps carried out at 2.5 mHz seem to be symmetric respect to -1 V and +1 V, relative to the steady baseline value the $\% \Delta \text{EOT}$ will reach at 0 V. The behavior observed for the following voltage ramps carried out at 6.25 mHz and 12.5 mHz (at ~ 4000 s and ~ 6000 s, respectively) is almost equivalent, except for the amplitude modulation of the optical signal, which decreases with increasing frequency. Besides, in spite of using lower bias and a sample with a higher carbon content, a gradual abatement in the baseline value is observed after each series of voltage ramps, revealing an overall small degradation of the sample over the time. However, the optical signal keeps a good correlation with the frequency modulation in every step (2.5 mHz, 6.25 mHz and 12.5 mHz) and the optical biosensor demonstrates to be thus sensitive to current sign changes in this window.

3.3.2 Negatively charged biomolecules

Bovine serum albumin (BSA) is a medium-sized molecule (14.0 nm X 3.8 nm X 3.8 nm, molecular mass ≈ 66 kDa) with an isoelectric point of 4.7. By using the same PBS buffer at pH 7.5, a clear negative charge distribution should surround the protein. Therefore, it would be expected to adsorb to a CPS electrode held at a positive bias. As formerly stated, Chen's samples exhibited significant corrosion at

values of $\Delta V \geq 0$, and no evidence of electroadsorption of BSA could be observed at positive bias values due to the instability of the electrode. In the next experiment, Figure 3-9, it is reported a test carried out with BSA by using the new CPS composites, in the case of a 20% sensor.

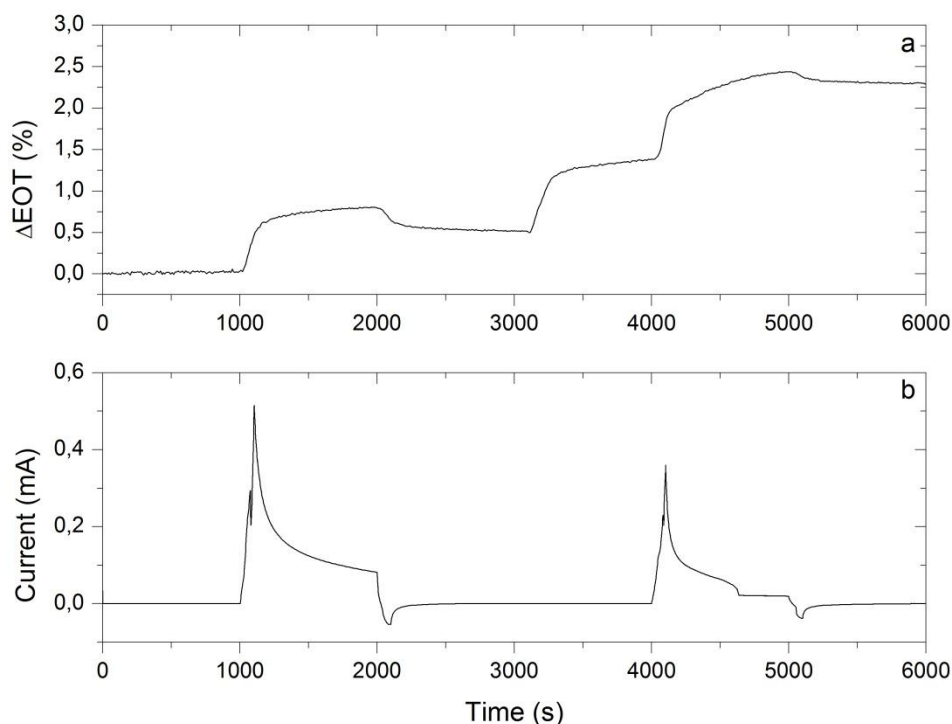


Figure 3-9 Optical (a) and electrical (b) responses of a 20% CPS sensor upon electric-field-assisted test with negatively charged BSA.

Timescales and parameters of the graphs from Figure 3-9 are similar to those of Figure 3-7. In this case, a positive bias (+1 V) was applied between time t_1 (1000 s) and t_2 (2000 s) and between time t_4 (4000 s) and t_5 (5000 s). During the remaining time, the CPS film was held at 0 V and BSA (10 mg mL^{-1}) was introduced at time t_3 (3000 s). The control made before adding proteins (t_1) reveals a large optical response of the sensor in pure buffer as a redshift of the order of 0.75% was measured. Moreover, as in the experiment of Figure 3-6, the value of $\% \Delta EOT$ does not return to the initial baseline value by setting the voltage back to 0 V (t_2),

suggesting that some ionic species were irreversibly adsorbed on the CPS surface. Infiltration of BSA (t_3) leads to a slight higher redshift compared, and approximately the same increase is observed upon application of the positive voltage (t_4), even if the profile is different. Again, as at time t_2 , a tiny blueshift can be detected setting the bias to 0 V (t_5), indicating that a very small quantity of negative charged species were released in these conditions. The fidelity in detection of electroadsorbed/desorbed negatively charged biomolecules can be in principle improved increasing the voltage applied, the protein concentration and by using a molecule with a lower isoelectric point. Pepsin is a medium-small enzyme (molecular weight ≈ 34.6 kDa) with an isoelectric point as low as 1.0. Graphs from Figure 3-10 refer to a test for which the molar concentration of negatively charged pepsin was greatly increased, trying to approach the one used for lysozyme in the experiments of Figures 3-7 and 3-8 (~ 700 μM). The results are again presented in the case of a 20% CPS sensor.

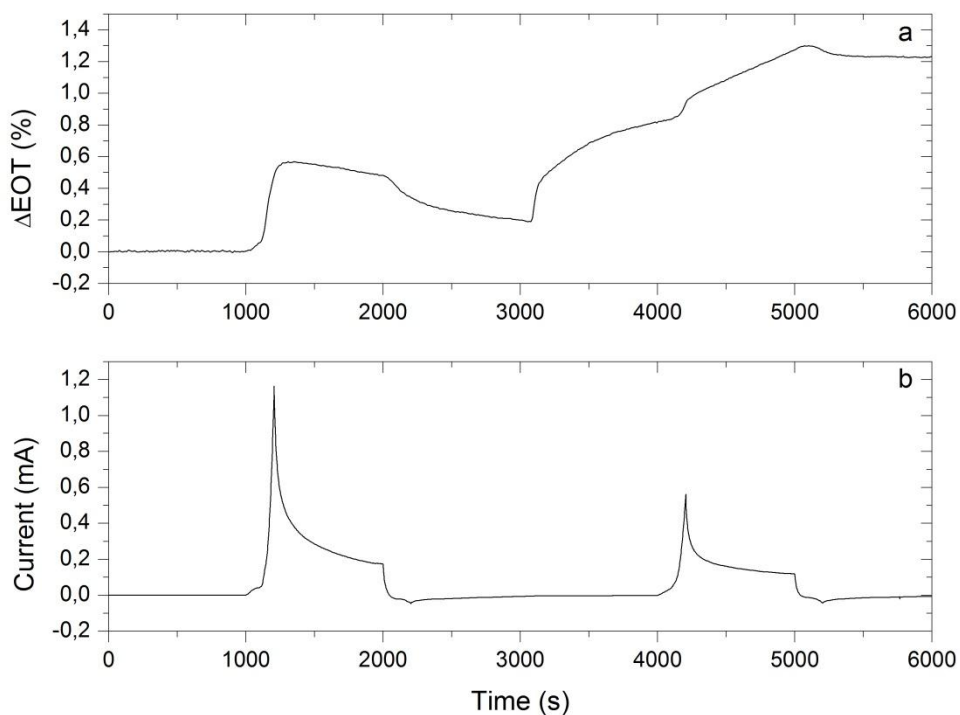


Figure 3-10 Optical (a) and electrical (b) responses of a 20% CPS sensor upon electric-field-assisted test with negatively charged pepsin.

Timescales and parameters of the graphs from Figure 3-10 are equivalent to those of Figure 3-9, except for the applied bias, which was increased up to +2 V. As it can be noted, the optical response of the sensor to pepsin is even lower than that with BSA, with witch shares, however, a similar behavior. A possible explanation can be found, in this case, in the pH of the PBS (7.5), as pepsin exhibits about 35% of its maximum activity at pH 4.5 already. Otherwise, as in the BSA case, it must be mainly taken into account the biocompatibility of the CPS surface, which can greatly contribute to the denaturation and deactivation of the biomolecules. In any case, the current vs time profile displays the same trend as in all the measurements presented, suggesting that a comparison based on the ratio between the different charging currents would be a better strategy, rather than further decreasing the ionic strength of the solution, to discriminate between contributions stemming from ions and biomolecules.

Conclusions

The stability in aqueous media of new nanostructured carbon/silicon composites, synthesized through the Kelly's carbonization chemistry, has been demonstrated, its dependence on the carbon content investigated in the range 1-25% by an optical method. Endurance and electrical conduction capabilities of the nanoelectrodes have been tried out under stress in liquid and upon application of different bias, both negative than positive. The measurements show encouraging results even for very low carbon quantities, suggesting their testing with higher carbon amounts, as well as with specific stability studies for energy harvesting applications, such as cyclic voltammetry. The feasibility to fabricate highly stable and sensitive optical interferometric sensors, based on electroadsorption as analyte capture technique, has been confirmed. Experiments with both negatively than positively charged biomolecular targets have been presented, and a parallel opto-electrochemical configuration has been set up to examine responses and performance of the device. Finally, an upgraded platform to identify biomolecules based on their size, charge, diffusional, and electrochemical characteristics has been proposed.

References

1. Watanabe Y, Arita Y, Yokoyama T, Igarashi Y: **FORMATION AND PROPERTIES OF POROUS SILICON AND ITS APPLICATION.** *Journal of the Electrochemical Society* 1975, **122**.
2. Ito T, Yamama A, Hiraki A, Satou M: **SILICIDATION OF POROUS SILICON AND ITS APPLICATION FOR THE FABRICATION OF A BURIED METAL LAYER.** *Applied Surface Science* 1989, **41-2**.
3. Anderson RC, Muller RS, Tobias CW: **INVESTIGATIONS OF POROUS SILICON FOR VAPOR SENSING.** *Sensors and Actuators a-Physical* 1990, **23**.
4. Canham LT: **SILICON QUANTUM WIRE ARRAY FABRICATION BY ELECTROCHEMICAL AND CHEMICAL DISSOLUTION OF WAFERS.** *Applied Physics Letters* 1990, **57**.
5. Lehmann V, Gosele U: **POROUS SILICON FORMATION - A QUANTUM WIRE EFFECT.** *Applied Physics Letters* 1991, **58**.
6. Hamilton B, Jacobs J, Hill DA, Pettifer RF, Teehan D, Canham LT: **Size-controlled percolation pathways for electrical conduction in porous silicon.** *Nature* 1998, **393**.
7. Stewart MP, Buriak JM: **Chemical and biological applications of porous silicon technology.** *Advanced Materials* 2000, **12**:859-869.
8. Singh N, Karambelkar A, Gu L, Lin K, Miller JS, Chen CS, Sailor MJ, Bhatia SN: **Bioresponsive Mesoporous Silica Nanoparticles for Triggered Drug Release.** *Journal of the American Chemical Society* 2011, **133**.
9. Lin VSY, Motesharei K, Dancil KPS, Sailor MJ, Ghadiri MR: **A porous**

- silicon-based optical interferometric biosensor.** *Science* 1997, **278**.
10. Sailor MJ: **Porous Silicon in Practice.** *Wiley-VCH Verlag & Co. KGaA* 2012.
 11. Anglin EJ, Schwartz MP, Ng VP, Perelman LA, Sailor MJ: **Engineering the chemistry and nanostructure of porous Silicon Fabry-Perot films for loading and release of a steroid.** *Langmuir* 2004, **20**.
 12. Theiss W, Henkel S, Arntzen M: **CONNECTING MICROSCOPIC AND MACROSCOPIC PROPERTIES OF POROUS-MEDIA - CHOOSING APPROPRIATE EFFECTIVE-MEDIUM CONCEPTS.** *Thin Solid Films* 1995, **255**.
 13. Wu J, Sailor M: **Chitosan Hydrogel-Capped Porous SiO₂ as a pH Responsive Nano-Valve for Triggered Release of Insulin.** *Advanced Functional Materials* 2009, **19**.
 14. Pacholski C, Perelman LA, VanNieuwenhze MS, Sailor MJ: **Small molecule detection by reflective interferometric Fourier transform spectroscopy (RIFTS).** *Physica Status Solidi a-Applications and Materials Science* 2009, **206**.
 15. Pacholski C, Yu C, Miskelly GM, Godin D, Sailor MJ: **Reflective interferometric Fourier transform spectroscopy: A self-compensating label-free immunosensor using double-layers of porous SiO₂.** *Journal of the American Chemical Society* 2006, **128**.
 16. Pacholski C, Sartor M, Sailor MJ, Cunin F, Miskelly GM: **Biosensing using porous silicon double-layer interferometers: Reflective interferometric Fourier transform spectroscopy.** *Journal of the American Chemical Society* 2005, **127**.

17. Mun K-S, Alvarez SD, Choi W-Y, Sailor MJ: **A Stable, Label-free Optical Interferometric Biosensor Based on TiO₂ Nanotube Arrays.** *Acs Nano* 2010, **4**.
18. Schwartz MP, Alvarez SD, Sailor MJ: **Porous SiO₂ interferometric biosensor for quantitative determination of protein interactions: Binding of protein a to immunoglobulins derived from different species.** *Analytical Chemistry* 2007, **79**.
19. Alvarez SD, Li C-P, Chiang CE, Schuller IK, Sailor MJ: **A Label-Free Porous Alumina Interferometric Immunosensor.** *Acs Nano* 2009, **3**.
20. Chen MY, Klunk MD, Diep VM, Sailor MJ: **Electric-Field-Assisted Protein Transport, Capture, and Interferometric Sensing in Carbonized Porous Silicon Films.** *Advanced Materials* 2011, **23**.
21. Rao AV, Ozanam F, Chazalviel JN: **INSITU FOURIER-TRANSFORM ELECTROMODULATED INFRARED STUDY OF POROUS SILICON FORMATION - EVIDENCE FOR SOLVENT EFFECTS ON THE VIBRATIONAL LINEWIDTHS.** *Journal of the Electrochemical Society* 1991, **138**:153-159.
22. Salonen J, Bjorkqvist M, Laine E, Niinisto L: **Stabilization of porous silicon surface by thermal decomposition of acetylene.** *Applied Surface Science* 2004, **225**.
23. Salonen J, Laine E, Niinisto L: **Thermal carbonization of porous silicon surface by acetylene.** *Journal of Applied Physics* 2002, **91**.
24. Salonen J, Lehto VP, Bjorkqvist M, Laine E, Niinisto L: **Studies of thermally-carbonize porous silicon surfaces.** *Physica Status Solidi a-Applied Research* 2000, **182**.

25. Bjorkqvist M, Paski J, Salonen J, Lehto VP: **Temperature dependence of thermally-carbonized porous silicon humidity sensor.** *Physica Status Solidi a-Applications and Materials Science* 2005, **202**.
26. Bjorkqvist M, Salonen J, Laine E: **Humidity behavior of thermally carbonized porous silicon.** *Applied Surface Science* 2004, **222**.
27. Bjorkqvist M, Salonen J, Paski J, Laine E: **Characterization of thermally carbonized porous silicon humidity sensor.** *Sensors and Actuators a-Physical* 2004, **112**.
28. Jalkanen T, Torres-Costa V, Salonen J, Bjorkqvist M, Makila E, Martinez-Duart JM, Lehto V-P: **Optical gas sensing properties of thermally hydrocarbonized porous silicon Bragg reflectors.** *Optics Express* 2009, **17**.
29. Salonen J, Tuura J, Bjorkqvist M, Lehto VP: **Sub-ppm trace moisture detection with a simple thermally carbonized porous silicon sensor.** *Sensors and Actuators B-Chemical* 2006, **114**.
30. Kaukonen AM, Laitinen L, Salonen J, Tuura J, Heikkila T, Linnell T, Hirvonen J, Lehto V-P: **Enhanced in vitro permeation of furosemide loaded into thermally carbonized mesoporous silicon (TCPSi) microparticles.** *European Journal of Pharmaceutics and Biopharmaceutics* 2007, **66**.
31. Heikkila T, Salonen J, Tuura J, Kumar N, Salmi T, Murzin DY, Hamdy MS, Mul G, Laitinen L, Kaukonen AM, et al: **Evaluation of mesoporous TCPSi, MCM-41, SBA-15, and TUD-1 materials as API carriers for oral drug delivery.** *Drug Delivery* 2007, **14**.
32. Bjorkqvist M, Salonen J, Laine E, Niinisto L: **Comparison of stabilizing treatments on porous silicon for sensor applications.** *Physica Status Solidi*

- a-Applied Research* 2003, **197**.
33. Salonen J, Kaukonen AM, Hirvonen J, Lehto V-P: **Mesoporous silicon in drug delivery applications.** *Journal of Pharmaceutical Sciences* 2008, **97**.
34. Salonen J, Laitinen L, Kaukonen AM, Tuura J, Bjorkqvist M, Heikkila T, Vaha-Heikkila K, Hirvonen J, Lehto VP: **Mesoporous silicon microparticles for oral drug delivery: Loading and release of five model drugs.** *Journal of Controlled Release* 2005, **108**.
35. Lehto VP, Vaha-Heikkila K, Paski J, Salonen J: **Use of thermoanalytical methods in quantification of drug load in mesoporous silicon microparticles.** *Journal of Thermal Analysis and Calorimetry* 2005, **80**.
36. Salonen J, Paski J, Vaha-Heikkila K, Heikkila T, Bjorkqvist M, Lehto VP: **Determination of drug load in porous silicon microparticles by calorimetry.** *Physica Status Solidi a-Applications and Materials Science* 2005, **202**.
37. Ruminski AM, King BH, Salonen J, Snyder JL, Sailor MJ: **Porous Silicon-Based Optical Microsensors for Volatile Organic Analytes: Effect of Surface Chemistry on Stability and Specificity.** *Advanced Functional Materials* 2010, **20**.
38. Mostofizadeh A, Li Y, Song B, Huang Y: **Synthesis, Properties, and Applications of Low-Dimensional Carbon-Related Nanomaterials.** *Journal of Nanomaterials* 2011.
39. Pandolfo AG, Hollenkamp AF: **Carbon properties and their role in supercapacitors.** *Journal of Power Sources* 2006, **157**.
40. Lokhande CD, Dubal DP, Joo O-S: **Metal oxide thin film based supercapacitors.** *Current Applied Physics* 2011, **11**.

41. Ghenaatian HR, Mousavi MF, Rahmanifar MS: **High performance hybrid supercapacitor based on two nanostructured conducting polymers: Self-doped polyaniline and polypyrrole nanofibers.** *Electrochimica Acta* 2012, **78**.
42. Merlet C, Rotenberg B, Madden PA, Taberna P-L, Simon P, Gogotsi Y, Salanne M: **On the molecular origin of supercapacitance in nanoporous carbon electrodes.** *Nature Materials* 2012, **11**.
43. Lufrano F, Staiti P: **Mesoporous Carbon Materials as Electrodes for Electrochemical Supercapacitors.** *International Journal of Electrochemical Science* 2010, **5**.
44. Park HG, Hwang S, Lim J, Kim D-H, Song IS, Kim JH, Woo DH, Lee S, Jun SC: **Comparison of Chemical Vapor Sensing Properties between Graphene and Carbon Nanotubes.** *Japanese Journal of Applied Physics* 2012, **51**.
45. Zuo J, Yao W, Liu X, Qin J: **Sensing Properties of Carbon Nanotube-Carbon Fiber/Cement Nanocomposites.** *Journal of Testing and Evaluation* 2012, **40**.
46. McDonough JR, Choi JW, Yang Y, La Mantia F, Zhang Y, Cui Y: **Carbon nanofiber supercapacitors with large areal capacitances.** *Applied Physics Letters* 2009, **95**.
47. Izadi-Najafabadi A, Yasuda S, Kobashi K, Yamada T, Futaba DN, Hatori H, Yumura M, Iijima S, Hata K: **Extracting the Full Potential of Single-Walled Carbon Nanotubes as Durable Supercapacitor Electrodes Operable at 4 V with High Power and Energy Density.** *Advanced Materials* 2010, **22**.

48. Frackowiak E, Metenier K, Bertagna V, Beguin F: **Supercapacitor electrodes from multiwalled carbon nanotubes.** *Applied Physics Letters* 2000, **77**.
49. Liu C, Yu Z, Neff D, Zhamu A, Jang BZ: **Graphene-Based Supercapacitor with an Ultrahigh Energy Density.** *Nano Letters* 2010, **10**.
50. Thakur M, Pernites RB, Nitta N, Isaacson M, Sinsabaugh SL, Wong MS, Biswal SL: **Freestanding Macroporous Silicon and Pyrolyzed Polyacrylonitrile As a Composite Anode for Lithium Ion Batteries.** *Chemistry of Materials* 2012, **24**.
51. Zhao Y, Liu X, Li H, Zhai T, Zhou H: **Hierarchical micro/nano porous silicon Li-ion battery anodes.** *Chemical Communications* 2012, **48**.
52. Guo J, Sun A, Wang C: **A porous silicon-carbon anode with high overall capacity on carbon fiber current collector.** *Electrochemistry Communications* 2010, **12**.
53. Astrova EV, Fedulova GV, Smirnova IA, Remenyuk AD, Kulova TL, Skundin AM: **Porous silicon based negative electrodes for lithium ion batteries.** *Technical Physics Letters* 2011, **37**.
54. Wang C-M, Li X, Wang Z, Xu W, Liu J, Gao F, Kovarik L, Zhang J-G, Howe J, Burton DJ, et al: **In Situ TEM Investigation of Congruent Phase Transition and Structural Evolution of Nanostructured Silicon/Carbon Anode for Lithium Ion Batteries.** *Nano Letters* 2012, **12**.
55. Cui L-F, Yang Y, Hsu C-M, Cui Y: **Carbon-Silicon Core-Shell Nanowires as High Capacity Electrode for Lithium Ion Batteries.** *Nano Letters* 2009, **9**.
56. Zhao C, Li Q, Wan W, Li J, Li J, Zhou H, Xu D: **Coaxial carbon-silicon-**

- carbon nanotube arrays in porous anodic aluminum oxide templates as anodes for lithium ion batteries.** *Journal of Materials Chemistry* 2012, **22**.
57. Kelly TL, Gao T, Sailor MJ: **Carbon and Carbon/Silicon Composites Templated in Rugate Filters for the Adsorption and Detection of Organic Vapors.** *Advanced Materials* 2011, **23**.
58. Striemer CC, Gaborski TR, McGrath JL, Fauchet PM: **Charge- and size-based separation of macromolecules using ultrathin silicon membranes.** *Nature* 2007, **445**.
59. Han J, Fu J, Schoch RB: **Molecular sieving using nanofilters: Past, present and future.** *Lab on a Chip* 2008, **8**.
60. Abgrall P, Nguyen NT: **Nanofluidic devices and their applications.** *Analytical Chemistry* 2008, **80**.
61. Basore JR, Lavrik NV, Baker LA: **Single-Pore Membranes Gated by Microelectromagnetic Traps.** *Advanced Materials* 2010, **22**.
62. Tokarev I, Minko S: **Stimuli-Responsive Porous Hydrogels at Interfaces for Molecular Filtration, Separation, Controlled Release, and Gating in Capsules and Membranes.** *Advanced Materials* 2010, **22**.
63. Schoch RB, Bertsch A, Renaud P: **pH-Controlled diffusion of proteins with different pI values across a nanochannel on a chip.** *Nano Letters* 2006, **6**.
64. Orosco MM, Pacholski C, Sailor MJ: **Real-time monitoring of enzyme activity in a mesoporous silicon double layer.** *Nature Nanotechnology* 2009, **4**.
65. Rong G, Weiss SM: **Biomolecule size-dependent sensitivity of porous silicon sensors.** *Physica Status Solidi a-Applications and Materials Science* 2009, **206**.

66. Chen MY, Sailor MJ: **Charge-Gated Transport of Proteins in Nanostructured Optical Films of Mesoporous Silica.** *Analytical Chemistry* 2011, **83**.

Acknowledgements/Ringraziamenti

This material is based upon research supported by Scuola Interpolitecnica di Dottorato, Politecnico di Torino, INRIM, Nanofacility Piemonte (a laboratory supported by Compagnia di San Paolo), and UCSD. As it stems from a particularly large number of collaborations and projects, a lot of people must be acknowledged for all the works performed during this PhD.

First of all, I wish to express my deepest gratitude to three persons: Dr. Luca Boarino, Dr. Andrea M. Rossi and Prof. Michael J. Sailor. Their friendship over the years allows me to go on the other side of the world and it is the primary reason that made of San Diego one of the best experience of my life. Luca and Andrea taught me the fundamentals of research and how to deal with issues in nanotechnology, demonstrated unexpected consideration and trust on me, invaluable guidance and support in a way that now I consider them more friends than supervisors. More importantly, when I asked for a training abroad and in spite of being understaffed and overworked, they did not hesitate a second by catapulting me to learn from one of the best in this field. I will be always beholden to them for this. Professor Sailor welcomed me in his labs as well as at his home, lunches or dinners with warmth, congeniality and outstanding availability. Although he was busy or even saturated with different projects, he found the time for a weekly personal meeting which significantly contributed to increase my scientific awareness. Above all, I'm thanking Prof. Sailor for each "good job, Dario" he said. This really helped me and instilled in me the necessary confidence I needed and I usually lack in. It has been

great, fun and a privilege to have Luca, Andrea and Mike as my special masters and examples.

Secondly, I want to thank both my Italian than American “mentors” who directly faced my fat-head: Andrea M. Giovannozzi, Emanuele Enrico, Annalisa Nastro, Michelle Y. Chen and Chia-Chen Wu. Thank you guys for all your teachings, suggestions, help and smiles. I take the opportunity to thank all the present and former members of the Sailor’s research group too, in particular: Vinh M. Diep, Nobuhiro Yagi, Andrea Potocny, Alejandra Nieto, Matt Kinsella, James S. Ha and Luo Gu. Of course, I’m particularly grateful to all my colleagues and friends at INRIM with which I shared very nice moments, in particular: Roberto Rocci, Natascia M. De Leo, Federica Celegato, Matteo Fretto, Matteo Bruna, Stefano Borini and Giampiero Amato.

The official reviewing of this thesis was done by Prof. Claudia Pacholski and Professor Michael J. Sailor, who are gratefully acknowledged along with my academic tutor Prof. Fabrizio C. Pirri.

Infine, desidero ringraziare immensamente la mia famiglia per il supporto, l’affetto e l’incoraggiamento di questi anni, mio papà, mio fratello Max, Giorgia e i miei zii Nanni e Rosa. E ancora tutti i miei amici che mi sono sempre stati accanto, soprattutto nei momenti difficili. Anche questa tesi, ad ogni modo, è dedicata esclusivamente ad una sola persona. Grazie mamma, ti voglio bene.

Torino, February 2013.

Dario Imbraglio

PhD Publications and Awards

NANO EXPRESS

Open Access

Submicron machining and biomolecule immobilization on porous silicon by electron beam

Dario Imbraguglio*, Andrea Mario Giovannozzi, Annalisa Nastro and Andrea Mario Rossi

Abstract

Three-dimensional submicrometric structures and biomolecular patterns have been fabricated on a porous silicon film by an electron beam-based functionalization method. The immobilized proteins act as a passivation layer against material corrosion in aqueous solutions. The effects' dependence on the main parameters of the process (i.e., the electron beam dose, the biomolecule concentration, and the incubation time) has been demonstrated.

Keywords: Porous silicon, Electron beam, Lithography, Micromachining, Biomolecules

PACS: 87.85.Va

Background

Electron beam lithography (EBL) is known to be a pattern-designing technique of integrated electrical circuits, with writing resolution even down to tens of nanometers, which allows the fabrication of innovative and advanced devices for nanotechnological applications [1,2]. In EBL procedures, electron-sensitive polymeric resists are usually spun on top of samples' surfaces prior to irradiation in a scanning electron microscope (SEM). Depending on the nature of the resist, the irradiated geometry or its specular negative is used as a mask for subsequent material etching or deposition steps in order to obtain structures with nanometer-scale features. However, the EBL, when directly used to desorb chemical species from a surface, can be also exploited as a local functionalization method [3] to create molecular modified or biopatterns without employing any resist. This has been the case, for instance, of porous silicon (PS) surface-based biosensors [4].

PS is a silicon nanosponge produced by electrochemical etching of crystalline silicon in a hydrofluoric (HF) acid-containing solution. It is one of the most investigated structures in nanomaterials science due to some fascinating properties which can be harnessed in many applied research fields [5]. Morphological parameters of

PS matrices, i.e., pore sizes, porosity (voids-to-total volume ratio), and thickness, can be easily controlled just by varying the experimental electrochemical conditions (such as current density, HF concentration, or etching duration), allowing the use of PS for size-selective filtration or separation processes, drug delivery, or sensing applications.

The huge specific surface area (in the order of $200 \text{ m}^2/\text{cm}^3$) of PS is hydride-terminated in as-etched samples [6,7], and a well-established modification chemistry has been developed in the past years to selectively bind large amounts of different target analytes within the pores [8]. In so far as biological species are concerned, the immobilization of proteins [9], enzymes [10], and antibodies [11] on PS surfaces can be achieved by different techniques. Among the ones which allow submicrometric definitions, the EBL has already proved its capability in designing chemical and biopatterns solely on selected and very small region of PS [3,4], opening the possibility of future development of highly-sensitive nanobiosensors and multiplexed analysis based on this material. From this perspective, PS is a very convenient substrate for EBL processes because of its porous structure. Indeed, due to the lower quantity of Si atoms with respect to an equal volume of bulk Si, PS behaves as a low-density material and exhibits a reduced proximity effect [2], which is the main limitation factor in writing resolution with standard EBL-based methods. Moreover,

* Correspondence: d.imbraguglio@inrim.it
Thermodynamics Division, Istituto Nazionale di Ricerca Metrologica, Strada delle Cacce 91, Torino 10135, Italy

the absence of the polymeric resist during irradiation further contains the phenomenon because the only cause of overexposure of PS irradiated regions stems from secondary and backscattered electrons just coming from the underlying PS/Si substrate. This means that more defined and small patterned features can be, in principle, obtained by direct, i.e., not resist-mediated, irradiation of PS. Therefore, by combining EBL nanostructuring capabilities with those of PS whose pore dimensions can be varied from the macro- to the microscale (<2 nm), sophisticated optical nanostructures could, in principle, be fabricated, such as three-dimensional (3D) photonic crystals, waveguides, or optical gratings.

As far as the application of the direct EBL method on PS is concerned, some previous works have already demonstrated its capability in material structuring [12,13] as well as the feasibility to fabricate a reliable biosensor [4]. Different kinds of geometries had been patterned on PS surfaces, and the control of feature dimensions is possible by tuning the process parameters. Furthermore, proteins which were bound on PS surfaces by such a resistless EBL technique had been shown to retain their full functionality after the process and can act as bioreceptors for molecular and biomolecular analytes. We report on recent studies and advances on both sides, i.e., the (submicron) machining and the immobilization of biomolecules on PS. The obtained results let us discover a new and intriguing property of the interaction between biomolecular species and a solid-state nanomaterial which, to the best of our knowledge, has never been observed before.

Methods

PS single-layer films have been anodically etched from highly boron-doped single-crystal Si wafers <100> (resistivity ranging from 0.008 to 0.012 Ω cm) in a 1:2 solution of aqueous 50% HF/ethanol in volume; the electrochemical etching procedure is described in several papers [3-5]. Typically, a double-step etching/stop loop (consisting of 0.2-sec etching at a current density of 400 mA/cm² followed by a 10-sec stop etching time) was repeated, the number of times depending on the desired film thickness, using a Keithley 2400 SourceMeter (Keithley Instruments Inc., Cleveland, OH, USA). PS samples with thicknesses of 6.5 and 9 μ m were fabricated, with pore dimensions comprised in the mesoscale regime (approximately 20 to 50 nm) and porosity of about 80%, as confirmed by profilometric and SEM measurements. Anyway, no substantial differences related to the different thickness values of the samples or due to decreasing the current density to 300 mA/cm² were observed in the experimental results.

After dipping in an HF-based solution in order to remove the native silicon oxide layer, PS samples were introduced into the vacuum chamber of a FEI Quanta

3D (FEI Co., Hillsboro, OR, USA) field emission gun (FEG) SEM equipped with a nano pattern generator system (NPGS) 9.0 from J.C. Naby Lithography Systems (Bozeman, MT, USA). Simple rectangular geometries, formed by line series 0.8- μ m wide and 30- μ m long (spaced by a distance of 0.7 μ m), were written by NPGS on the PS sample surfaces, applying a 20-kV accelerating voltage to the electron beam. The electronic dose (i.e., the number of electrons per area units) range explored in this work has been varied from 40 up to 200 mC/cm².

In order to allow as much consistent comparison between samples as possible, identical patterns were written on specular portions of the same PS chip, which were then divided after irradiation and immediately immersed in buffered solutions. Depending on the test performed, pure 1 X phosphate buffered saline (PBS) or bovine serum albumin (BSA) protein-containing solutions were prepared. PBS tablets and BSA lyophilized powders from Sigma-Aldrich (St. Louis, MO, USA) have been dissolved in purified water provided by a Millipore Elix 3 purification system (Millipore Co., Billerica, MA, USA). The pH of pure PBS solutions has been checked each time by a CyberScan pH/Ion 510 meter (Eutech Instruments, Vernon Hills, IL, USA) to be equal to a nominal value of 7.4. Four different BSA concentrations (5, 1, 0.5, and 0.1 μ M) were obtained by multiple dilutions from a 15- μ M mother solution of BSA in PBS buffer. The irradiated PS samples were incubated for times ranging from 5 to 120 min, after which they were profusely rinsed first in PBS, then in deionized water and finally dried with nitrogen gas.

Fourier transform infrared (FTIR) reflectance spectra have been acquired using a Nicolet Nexus FTIR spectrophotometer (Thermo Scientific, Logan, UT, USA) coupled with a Nicolet Continuum FTIR microscope equipped with a MCT detector. The spectra were collected both in the irradiated area and just a few micrometers outside by registering a total of 512 interferograms for each spectrum with a resolution of 4 cm⁻¹. Finally, the samples were observed with a FEI Inspect F FEG SEM in a tilted (60°) secondary electron configuration.

Results and discussion

It is well known that high-surface-area nanomaterials such as PS undergo rapid oxidation and even dissolution when exposed to ambient air conditions or immersed in aqueous solutions because of their poor stability [14]. These kinds of processes can be locally further stressed and speeded up by using different techniques, such as laser writing [15,16] or contact atomic force microscopy-based methods [17]. From this point of view, EBL can potentially be used to remove material from a solid substrate only in submicrometer-wide regions due to the high focusing power of the electron beam. Among other different

approaches, EBL can be thought of as a good compromise in so far as writing speed and resolution are concerned. As previously mentioned, the interaction between PS and the electron beam has already been studied in some former works [3,4,12,13]. Rocchia et al. [3] first demonstrated that the electron irradiation provokes hydrogen desorption from the native SiH_x bonds of PS surfaces, leading to high reactive electron beam-activated PS (EBAPS) regions which easily oxidize in ambient air. Such a strong reactivity is most likely due to the formation of dangling bonds and defects as a consequence of the hydrogen depletion caused by the electron bombardment. Nevertheless, in the reported previous cases, even if the written geometries were clearly distinguishable immediately after irradiation by the electron microscope, optical, profilometric, and SEM investigations did not reveal any substantial structuring of the PS along the z -axis (perpendicular to the PS surface). Anyway, very tiny z -depth profiles were measured only after removing the electro-oxidized PS areas in acid or alkaline solutions, as the difference step between the top non-exposed PS surface and the bottom crystalline Si one after EBAPS removal. The amplitude of such thicknesses had been studied as a function of different oxidizing conditions (air, water, H_2O_2 , incubation time) as well as energies and electronic doses provided by the electron beam. The results showed that the stronger the oxidizing procedure is, the thicker is the depth measured by profilometry, and so the final vertical structuring of PS. Besides, monotonic increases in the thickness were observed by augmenting the electronic dose and the accelerating voltage of the electron beam. In the latter case, a 25-kV saturation value was found, beyond which the electrons lose their energy also through the Si bulk underlying the PS substrate, and the effect no longer depends on the electron energy. The maximum depth value (≈ 180 nm) was obtained with a 12- μm thick sample irradiated at 25 kV at the maximum electronic dose ($120 \text{ mC}/\text{cm}^2$) [13]. It has to be pointed out that the reported thickness values were detected only after dipping EBAPS samples in HF or KOH etchants. This is a quite aggressive etching procedure which may cause, in some case, the removal of PS non-exposed areas too due to the low degree of selectivity of such methods. Obviously, as far as micro- or nano-machining of PS is concerned, easiness and precise reproducibility in fabrication of machined structures are two important requirements.

Here, our new improvements and results about such a PS EBL-assisted structuring technique are reported. We decided to operate the electron beam with a lower accelerating voltage with respect to the previous cases in order to have a minor penetration depth of electrons through the PS layer. In spite of using high electronic doses even up to $200 \text{ mC}/\text{cm}^2$, we also have not noted any modification on the PS morphological structure just

after irradiation. The as-written geometries were barely visible at the optical microscope as well as at the SEM, where the exposed areas were distinguished, even after long storage in air, only by a slight contrast difference in the acquired images. On the other hand, after dipping the EBAPS samples in pure PBS for quite long incubation times, the patterned geometries resulted to be, after the process, as printed onto the PS matrix. Figure 1 displays a SEM tilted image of a sample irradiated with a very low electronic dose ($40 \text{ mC}/\text{cm}^2$) and immersed in a pure PBS solution for 1 h. The submicrometric irradiated strips are the void regions in the picture, and an accomplished structuring of the nanomaterial along the z -axis is evident. The porous matrix between one strip and another is maintained, revealing that such an erosion effect is doubtlessly caused by the combined action of the buffer only with the EBAPS regions. As we have said, EBL on as-etched PS samples induces hydrogen desorption from the surface, with the consequent formation of very reactive dangling bonds that tend to saturate with other atoms present in the environment, most commonly oxygen. However, PS oxidation in air is not strong enough to produce visible effects on the material, not even by increasing the electronic dose and, therefore, the number of EBAPS sites. In aqueous solutions such as PBS buffer, instead, water molecules can penetrate inside the nanopores, and oxygen atoms link to the EBAPS pore walls. The already weakened and unstable PS nanostructure is most likely further overburdened, and a selective electron beam-driven redox dissolution takes place, which slowly manifests itself in several-minutes-long timescales. In the present case, the corrosion by PBS starts to be noticeable only after about

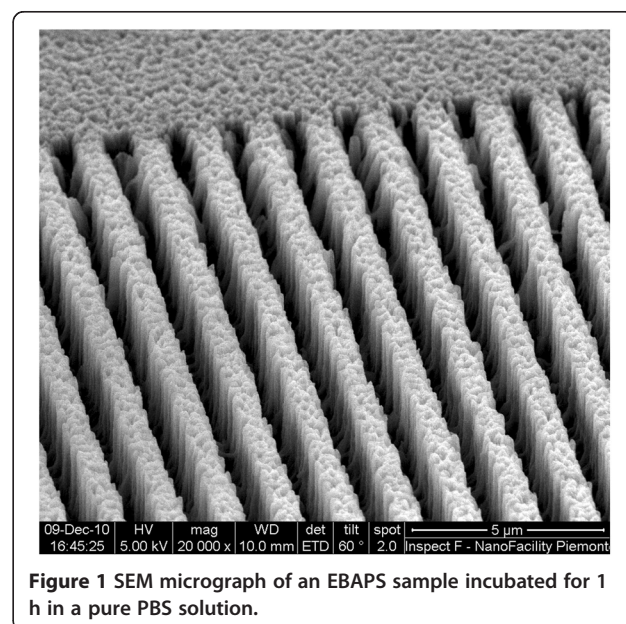


Figure 1 SEM micrograph of an EBAPS sample incubated for 1 h in a pure PBS solution.

20 min, while after incubation times up to 1 h, holes with depths of even few micrometers can be easily obtained. By exploiting this process, any 2D geometry can be propagated through the nanostructured 'PS bulk' in a way similar to what happens with other emerging bulk Si etching techniques, as for instance metal-assisted-based methods [18]. In the studied submicrometric regime, the 3D fabricated structures are very well defined, and the material removal can be simply controlled by varying the incubation time in an aqueous pH 7.4 or neutral solution.

More surprisingly, the phenomenon of PS dissolution is in some way limited by the presence of BSA biomolecules in the buffering solutions. As previously mentioned, the enhanced reactivity of EBAPS submicrometric regions can be harnessed to locally bind biomolecules or other chemical species only in the irradiated area. Nevertheless, the anchorage mechanism and dynamics in the solution are still not completely clear, and a deeper study of such immobilization process is currently in progress. As yet, the method seems to be not selective with respect to different biomolecular targets [4]; hence, a huge variety of possibilities can be, in principle, explored to further improve the chemical functionalization skills of PS. We used serum albumin from bovine blood as a test biomolecule since it is relatively small ($14 \times 3.8 \times 3.8 \text{ nm}^3$, molecular mass $\approx 66 \text{ kDa}$) [19] and able to penetrate inside the pores of our samples. Figure 2 shows a SEM tilted image of PS irradiated in the same conditions with that of the one displayed in Figure 1 but immersed in a $15\text{-}\mu\text{M}$ BSA-containing buffer solution. As clearly shown in Figure 2, the situation is completely different in comparison to the previous case. Here, the irradiated strips are still visible in

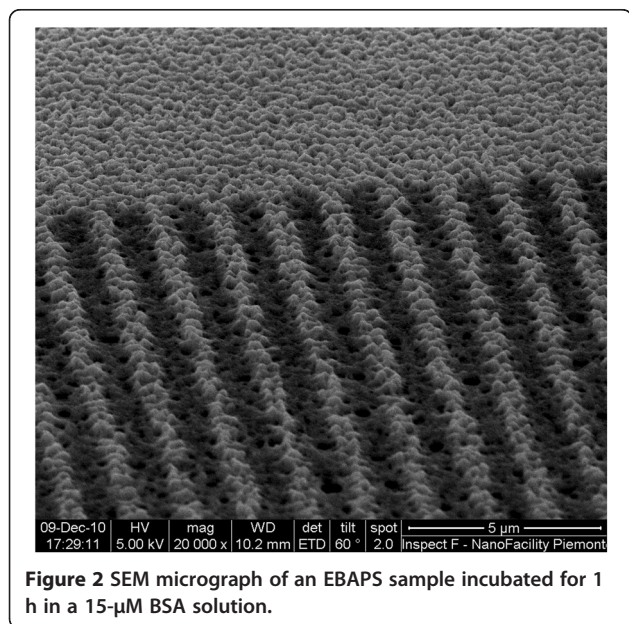


Figure 2 SEM micrograph of an EBAPS sample incubated for 1 h in a $15\text{-}\mu\text{M}$ BSA solution.

a SEM image as darker regions across the PS matrix, presumably due to changes in the electrical conductivity of the material, but the overall structure looks almost completely preserved.

In order to check the selective immobilization of BSA biomolecules on the PS surface, a systematic FTIR spectroscopic study has been carried out by collecting the reflected infrared radiation from the film inside and outside the EBAPS areas ($60 \mu\text{m} \times 30 \mu\text{m}$). This has been done in the same way for three different typologies of EBAPS samples: (a) EBAPS incubated for 1 h in a BSA-PBS solution, (b) EBAPS incubated for 1 h in a pure PBS solution, and (c) EBAPS left in air atmosphere for 1 day. Figure 3 summarizes the indicative behavior of all the samples by showing the FTIR spectra in the range of 800 to $2,300 \text{ cm}^{-1}$. Among the detectable vibrational mode signals, only those related to the adsorption bands of the Si-H_x groups ($2,000$ to $2,200 \text{ cm}^{-1}$ and 900 cm^{-1}), Si-O_x groups ($1,000$ to $1,100 \text{ cm}^{-1}$), and Amide I ($1,650 \text{ cm}^{-1}$) and Amide II ($1,550 \text{ cm}^{-1}$) BSA peptide bond [20] have been monitored. As it can be seen from Figure 3, each EBAPS spectrum displays an adsorption signal decrease, with respect to the control obtained outside, of Si-H stretching ($2,000$ to $2,200 \text{ cm}^{-1}$) and scissoring (900 cm^{-1}) modes in the electron-irradiated region, which is the hallmark of local hydrogen depletion due to the electron beam activation. It has to be specified that a part of such decrease is also ascribed to a complementary increase of vibrations related to oxidation ($1,000$ to $1,100 \text{ cm}^{-1}$) and, in the case of the samples exposed to the BSA, biomolecular bonding. As expected anyway, the Amide I and Amide II adsorption bands are clearly present only in the spectrum of the irradiated region in the first kind of samples (Figure 3a), meaning that a selective immobilization of proteins has been achieved. We plainly cannot exclude that some small quantities of BSA were also bound to the PS surface between one strip and the other since the FTIR resolution does not allow performing measurements in such a very small area. Nevertheless, the great lateral definition of the strips in Figure 2 suggests that the selective immobilization has been accomplished in the submicron range as well. More important is the different final degree of oxidation displayed by the samples in the spectra of Figure 3. The lowest variation in the Si-O absorption bands between irradiated and non-irradiated regions is the one related to EBAPS stored in air (Figure 3c) for which, as we have previously mentioned, any structural change in the material conformation was observed. This is also confirmed by the maintained periodicity of the Fabri-Pérot interference fringes of the irradiated area by comparing inside and outside regions in the spectra of Figure 3c. In EBAPS samples incubated for 1 h in a BSA-containing buffer solution (Figure 3a), the oxidation is higher but the structure of the PS film is still preserved (Figure 2). On

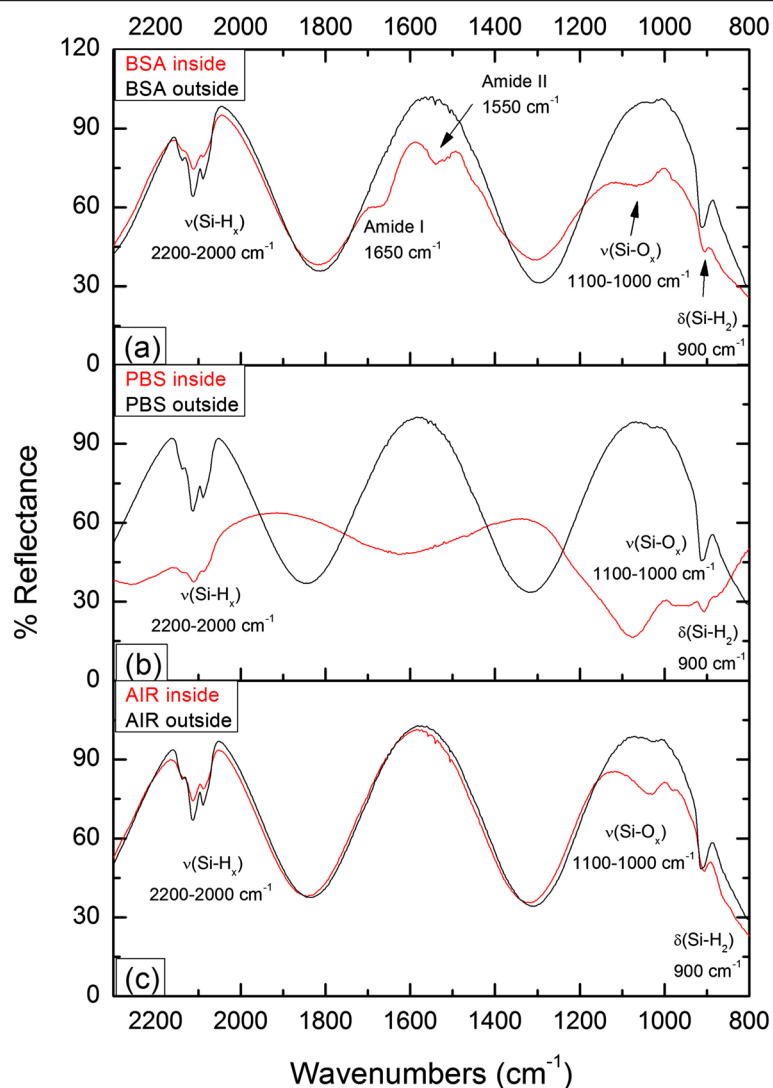


Figure 3 FTIR spectra of the EBAPS samples. EBAPS incubated for 1 h in a BSA-PBS solution (a), incubated for 1 h in a pure PBS solution (b), and stored in air for 1 day (c). For each window, the spectrum of the exposed area (red) is compared to the control obtained from the non-exposed one (black).

the other hand, the interference pattern uniformity in the FTIR spectra of the EBAPS samples which were left, for the same time, in a BSA-free solution is nearly lost (Figure 3b), and this situation corresponds to the morphological sight of the EBAPS reported in the SEM picture of Figure 1. In this case, the highest degree of oxidation is registered, which let us conclude that the immobilized BSA proteins are able to shield EBAPS surfaces from excessive oxygen binding and thus avoid redox dissolution processes of the PS matrix.

In the present case, the conservation of the Fabri-Pérot interference pattern uniformity has been used as a roundabout optical method to exclude that the preservation of the PS matrix, observed in Figure 2, was due to just a superficial passivation acted by the immobilized

proteins. BSA biomolecules are small enough to penetrate inside the nanopores of EBAPS samples as well as water molecules, whose number is, however, several orders of magnitude larger in a few micromolar concentrated BSA buffer solution. It is very unlikely that BSA molecules could directly bind to the activated Si sites through a covalent bond because of, firstly, the highest probability which water molecules have to saturate with EBAPS dangling bonds. Secondly, it had been demonstrated in few cases that the biomolecular functionality of the immobilized target is retained after the process [4], and such a kind of attachment would rather denature the biomolecule of interest. On the other hand, the strong affinity of BSA for Si dioxide is well established [21], and it is therefore plausible that oxygen

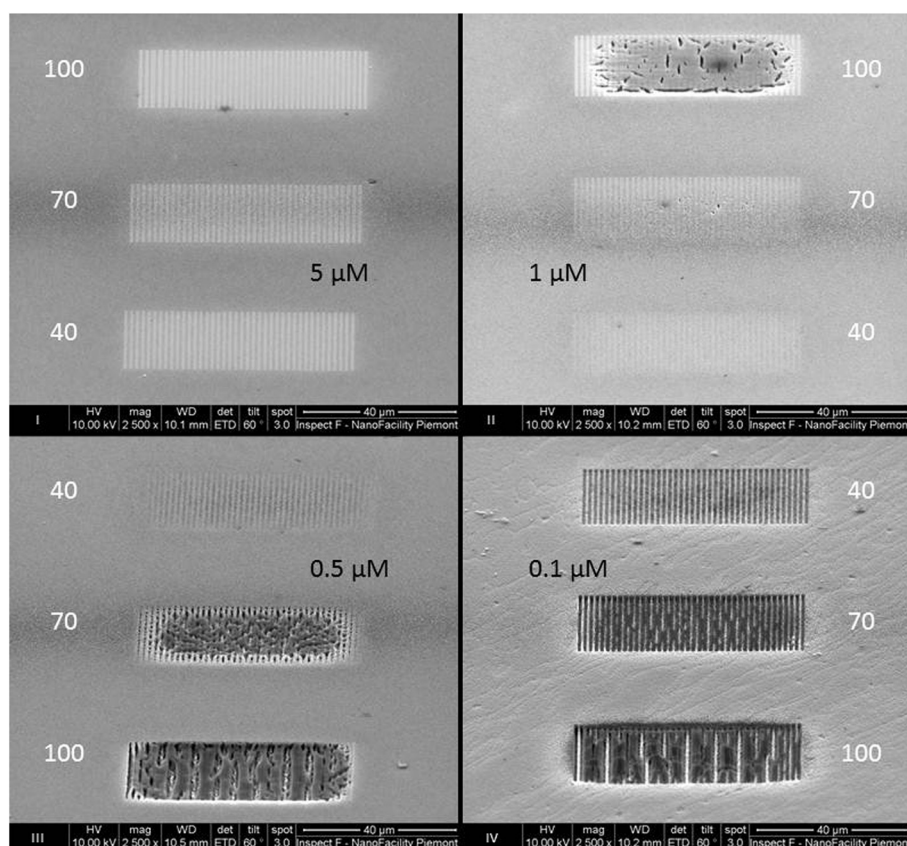


Figure 4 SEM micrographs of four electron-irradiated regions (I, II, III, and IV) of a PS sample. Taken after 1-h exposure to distinct BSA solutions. The protein concentrations are indicated (black), as well the increase of the electron beam dose from 40 up to 100 mC/cm² (white).

atoms could act also as a linker for the immobilization of BSA proteins to the EBAPS pore walls. During the incubation time of the EBAPS samples with the BSA solution, two fast reactions probably occurred one after the other: the enhanced oxidation of the irradiated areas and the consequent selective attachment of BSA molecules to these regions. As soon as the reaction proceeds, the constrained space available within the nanopores favors the packaging of the biomolecules, thus creating a sort of scaffold which prevents material corrosion. In this way, a soft matrix as that formed by the BSA proteins is able to protect and sustain a nanostructured solid one.

An interaction mechanism like the one we just described should firstly depend on the initial concentration of biomolecular species in the solution. In addition, considering the dependence of the oxidation on the SEM operating conditions, the PS dissolution process may be further amplified by increasing the electron accelerating voltage or the electronic dose supplied by the electron beam [12,13]. In order to find a final confirmation of that, EBAPS samples were incubated in four protein buffer solutions, each one containing a different concentration of BSA: 5, 1, 0.5, and 0.1 μM. We chose

to keep fixed the accelerating voltage at 20 kV and to vary for each sample the electronic dose from 40 up to 70 mC/cm² in order to facilitate quantitative evaluations. Figure 4 groups the SEM tilted images of the four irradiated portions (I, II, III, and IV quadrants in Figure 4) after 1 h of incubation time. Concentration and electronic dose values are indicated in black and white in the figure, respectively. The selective immobilization of BSA and the interferometric pattern features have been even checked in this case by FTIR spectroscopy measurements, which are not reported here. In the reported SEM magnifications, at the highest BSA concentration (5 μM), the biomolecular patterns fabricated by the EBL technique appear as bright strips through the PS matrix (Figure 4, quadrant I). We noted a tiny increase in the strips' breadth by augmenting the electronic dose in such range, which is simply due to a greater proximity effect occurring at high electron beam irradiation conditions. Anyway, the strips are disconnected from one another in every pattern irradiated with a different electronic dose, even at 100 mC/cm², and the submicrometric definition can be achieved by using the lowest one. The situation displayed by the sample incubated in

a solution with a lower concentration of BSA (1 μM) is nearly similar (Figure 4, quadrant II), except for some cracks and several-micrometer-square-wide holes which start to compromise the PS structure at the 100-mC/cm² electronic dose. Since these features are not present at 70 mC/cm² as well as at 40 mC/cm², this proves that a higher electronic dose of the electron beam causes greater stress and degradation of the porous material. By further decreasing the BSA concentration down to 0.5 μM , the aspect of the EBAPS samples drastically changes (Figure 4, quadrant III). Here, machined structures begin to form in each electronic dose case. The submicrometric resolution is only accomplished at 40 mC/cm², and PS coalescence phenomena between non-irradiated areas seem to take place at the medium electronic dose, after which the entire exposed and non-exposed regions collapse at the maximum dose. Such a loss of writing resolution is again caused by the increasing proximity effect, which is even more evident by reducing the amount of biomolecules down to the lowest concentration value (0.1 μM ; Figure 4, quadrant IV). As it happens in complete absence of biomolecules in the solution (Figure 1), very well-defined rectangular strips that cross the material matrix are produced, in this case, only by using an electronic dose of 40 mC/cm², which seems to be the optimum value to fabricate both submicrometric biomolecular patterns as well as free-standing PS structures. By comparing all the SEM pictures of Figure 4, we therefore demonstrated that the degree of passivation from the electron beam-driven PS dissolution can be controlled by tuning the molar concentration of proteins in solution. Anyway, above a threshold value of 1 μM , the overall EBAPS structure is preserved even at high electronic doses, and stable submicrometric biomolecular patterns can be easily realized. These observations are consistent with some recently published results about the modification of crystalline silicon surfaces by bioactive films of proteins [22], which allow the fabrication of advanced biocompatible hybrid systems. The advantage of our approach lies in the capability to obtain the same passivation effects on an already nanostructured and hence weaker material.

Conclusions

We found that electron beam irradiation on PS has no noticeable effects on its morphological structure as long as, after EBL writing, samples were left in air or just a few minutes in buffered solutions. On the other hand, if the irradiated PS samples were dipped for incubation times greater than 20 min in pure PBS (or very low BSA concentrated) solutions, the irradiated strips appear, after drying, as well-defined submicrometric vertical structures embedded into the porous matrix, suggesting that a heavy EBL-controlled erosion of the nanomaterial

can be accomplished in these conditions. A valuable option to common 3D micro- and nano-machining techniques of PS has thus been proposed.

In addition, submicrometric bio-PS composite patterns have been successfully fabricated by the same technique, and a nanoscale biomolecular passivation effect has also been observed. We are confident to transfer the acquired knowledge to the immobilization of other and more useful nano and biomolecular targets (i.e., conductive biomolecules or functionalized metallic nanoparticles), which could be suitable for applications in different emerging research fields, such as molecular and bioelectronics or surface-enhanced Raman spectroscopy.

Competing interests

The authors declare that they have no competing interests.

Authors' contributions

DI carried out the fabrication of the PS samples, the EBL processes, the FTIR characterization, and drafting of the manuscript. AMG participated in the fabrication of the PS samples and FTIR characterization. AN participated in the FTIR characterization. AMR coordinated the study. All authors read and approved the final manuscript.

Acknowledgments

This work has been performed at Nano Facility Piemonte, INRiM, a laboratory supported by Compagnia di San Paolo. The authors thank Emanuele Enrico and Luca Boarino for their support.

Received: 30 April 2012 Accepted: 13 September 2012

Published: 25 September 2012

References

1. Vieu C, Carcenac F, Pepin A, Chen Y, Mejias M, Lebib A, Manin-Ferlazzo L, Couraud L, Launois H: **Electron beam lithography: resolution limits and applications.** *Appl Surf Sci* 2000, **164**:111–117.
2. Tseng AA, Chen K, Chen CD, Ma KJ: **Electron beam lithography in nanoscale fabrication: recent development.** *IEEE Trans Electron Packag Manuf* 2003, **26**:141–149.
3. Rocchia M, Borini S, Rossi AM, Boarino L, Amato G: **Submicrometer functionalization of porous silicon by electron beam lithography.** *Adv Mater* 2003, **15**:1465–1469.
4. Borini S, D'Auria S, Rossi M, Rossi AM: **Writing 3D protein nanopatterns onto a silicon nanosponge.** *Lab Chip* 2005, **5**:1048–1052.
5. Cullis AG, Canham LT, Calcott PDJ: **The structural and luminescence properties of porous silicon.** *J Appl Phys* 1997, **82**:909–965.
6. Rao AV, Ozanam F, Chazalviel JN: **In situ Fourier-transform electromodulated infrared study of porous silicon formation - evidence for solvent effects on the vibrational linewidths.** *J Electrochem Soc* 1991, **138**:153–159.
7. Stievenard D, Deresmes D: **Are electrical properties of an aluminum-porous silicon junction governed by dangling bonds.** *Appl Phys Lett* 1995, **67**:1570–1572.
8. Stewart MP, Buriak JM: **Chemical and biological applications of porous silicon technology.** *Adv Mater* 2000, **12**:859–869.
9. Dancil KPS, Greiner DP, Sailor MJ: **A porous silicon optical biosensor: detection of reversible binding of IgG to a protein A-modified surface.** *J Am Chem Soc* 1999, **121**:7925–7930.
10. Letant SE, Hart BR, Kane SR, Hadi MZ, Shields SJ, Reynolds JG: **Enzyme immobilization on porous silicon surfaces.** *Adv Mater* 2004, **16**:689+.
11. Rossi AM, Wang L, Reipa V, Murphy TE: **Porous silicon biosensor for detection of viruses.** *Biosens Bioelectron* 2007, **23**:741–745.
12. Borini S, Amato G, Rocchia M, Boarino L, Rossi AM: **Electron-beam irradiation of porous silicon: application to micromachining.** *J Appl Phys* 2003, **93**:4439–4441.

13. Borini S, Rocchia M, Rossi AM, Boarino L, Amato G: **Electron beam irradiation of porous silicon for application in micromachining and sensing.** *Physica Status Solidi a-Applications and Materials Science* 2005, **202**:1648–1652.
14. Petrova EA, Bogoslovskaya KN, Balagurov LA, Kochoradze GI: **Room temperature oxidation of porous silicon in air.** *Materials Science and Engineering B-Solid State Materials for Advanced Technology* 2000, **69**:152–156.
15. Rossi AM, Amato G, Camarchia V, Boarino L, Borini S: **High-quality porous-silicon buried waveguides.** *Appl Phys Lett* 2001, **78**:3003–3005.
16. De Stefano L, Rea I, Nigro MA, Della Corte FG, Rendina I: **A parametric study of laser induced ablation-oxidation on porous silicon surfaces.** *J Phys Condens Matter* 2008, **20**:265009.
17. Wouters D, Schubert US: **Nanolithography and nanochemistry: probe-related patterning techniques and chemical modification for nanometer-sized devices.** *Angew Chem Int Ed* 2004, **43**:2480–2495.
18. Boarino L, Enrico E, De Leo N, Celegato F, Tiberto P, Sparnacci K, Laus M: **Macro and quasi-mesoporous silicon by self-assembling and metal assisted etching.** *Physica Status Solidi a-Applications and Materials Science* 2011, **208**:1403–1406.
19. Chen MY, Sailor MJ: **Charge-gated transport of proteins in nanostructured optical films of mesoporous silica.** *Anal Chem* 2011, **83**:7186–7193.
20. Noinville S, Revault M, Baron MH, Tiss A, Yapoudjian S, Ivanova M, Verger R: **Conformational changes and orientation of Humicola lanuginosa lipase on a solid hydrophobic surface: an in situ interface Fourier transform infrared-attenuated total reflection study.** *Biophys J* 2002, **82**:2709–2719.
21. Su TJ, Lu JR, Thomas RK, Cui ZF: **Effect of pH on the adsorption of bovine serum albumin at the silica water interface studied by neutron reflection.** *J Phys Chem B* 1999, **103**:3727–3736.
22. De Stefano L, Rea I, De Tommasi E, Rendina I, Rotiroli L, Giocondo M, Longobardi S, Armenante A, Giardina P: **Bioactive modification of silicon surface using self-assembled hydrophobins from Pleurotus ostreatus.** *European Physical Journal E* 2009, **30**:181–185.

doi:10.1186/1556-276X-7-530

Cite this article as: Imbraguglio *et al.*: Submicron machining and biomolecule immobilization on porous silicon by electron beam. *Nanoscale Research Letters* 2012 **7**:530.

Submit your manuscript to a SpringerOpen[®] journal and benefit from:

- ▶ Convenient online submission
- ▶ Rigorous peer review
- ▶ Immediate publication on acceptance
- ▶ Open access: articles freely available online
- ▶ High visibility within the field
- ▶ Retaining the copyright to your article

Submit your next manuscript at ▶ springeropen.com

Fabrication of ordered silicon nanopillars and nanowires by self-assembly and metal-assisted etching

Luca Boarino^{*1}, Dario Imbraguglio¹, Emanuele Enrico¹, Natascia De Leo¹, Federica Celegato¹, Paola Tiberto¹, Nicola Pugno², and Giampiero Amato¹

¹NanoFacility Piemonte, Electromagnetism Division, Istituto Nazionale di Ricerca Metrologica, Strada delle Cacce 91, 10135 Turin, Italy

²Laboratory of Bio-inspired Nanomechanics “Giuseppe Maria Pugno”, Department of Structural and Geotechnical Engineering, Politecnico di Torino, C.so Duca degli Abruzzi 24, 10129 Turin, Italy

Received 29 April 2010, revised 30 October 2010, accepted 24 November 2010

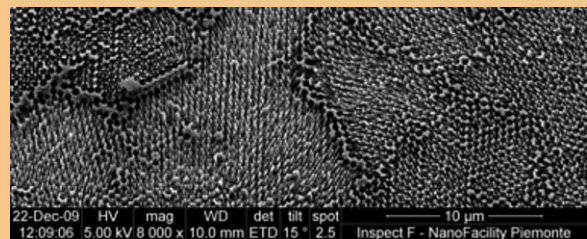
Published online 18 March 2011

Keywords metal-assisted etching, nanopillars, nanowires, self-assembly, silicon

* Corresponding author: e-mail l.boarino@inrim.it, Phone: +39 11 3919343, Fax: +39 11 346384

Silicon nanowires (SiNWs) and nanopillars have been obtained by metal-assisted etching (MAE), starting from silver thin films deposited by thermal evaporation and sputtering on silicon substrates. Different deposition methods and thickness are strongly affecting spatial distribution and shapes of the extruded silicon nanostructures. The paper reports a study of distribution and morphology, as a function of silver thickness, deposition conditions and etching times. The application of polystyrene soft masks obtained by self-assembly and the sputter-etching by Ar ions allow the formation of regular indentations in the silver thin films, giving origin to a regular distribution of extruded pillars and wires during the following etching in HF:H₂O₂:H₂O. The aqueous etching and the use of silver still influence the homogeneity of the etching result on large area and introduce a modulation in the etching front, so

affecting thickness homogeneity. Work is in progress to replicate these former results with gold and different etching solutions.



SEM microphoto of ordered SiNWs obtained by MAE and polystyrene nanosphere self-assembly.

© 2011 WILEY-VCH Verlag GmbH & Co. KGaA, Weinheim

1 Introduction The field of silicon nanowires (SiNWs) saw, in the last years, a real boom in the number and quality of publications. A part the basic research, investigating fundamental properties like electron transport [1] and mechanics [2], several fields of application can take advantage from SiNWs, like photovoltaic energy production by means of new generation devices [3], energy harvesting by vibrations [4] and new adhesives [5].

The recent development of self-catalytic electroless etching in presence of metals [6], offers a new degree of freedom in nanofabrication, because this kind of etching is only slightly dependent on silicon wafer doping and from solutions and etching conditions [7] but mainly from metal

distribution, thickness or patterning at the silicon surface. We used these different conditions, from continuous thin silver films deposited by different methods and with different thickness to obtain a nanopatterning of thin silver films by means of self-assembled monolayers of polystyrene nanospheres (PSNS). In this way it is possible to obtain forests of SiNWs with different spatial density, distribution and order.

2 Experimental results and discussion Silicon wafers by MEMC Corporation, $\langle 100 \rangle$ 20–30 Ω cm have been cleaned by RCA for 1 h to remove organic contamination, and then silver thin films of different thickness (20, 30

© 2011 WILEY-VCH Verlag GmbH & Co. KGaA, Weinheim

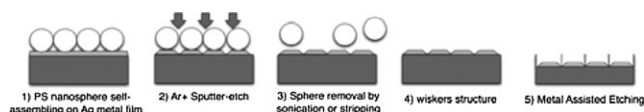


Figure 1 Processing steps for SiNWs and nanopillars fabrication by MAE and PSNS self-assembly.

and 40 nm) have been obtained by thermal evaporation or sputtering with typical conditions are of 50 W RF power and Ar^+ pressure of 10^{-2} mbar. SEM investigations have been performed by a FEI Inspect F to check thin film quality. Subsequently, a large 2D crystal of Sigma–Aldrich 500 nm PSNS has been self-assembled and carefully lifted on the substrate. After drying, sputter etching by Ar^+ ions is performed, with RF power of 100 W, Ar^+ pressure of 10^{-2} mbar and with times ranging from 1 to 3 min (processing steps sketched in Fig. 1), to obtain a silver film with regular indentation favouring the extrusion of silicon nanopillars and nanowires in the following etching step.

After sputter-etching, nanospheres have been removed by sonication in hot acetone or toluene. At this point metal-assisted etching (MAE) has then been performed for all the samples for with times ranging from 10 to 60 s at 60 °C in a solution of $\text{HF}:\text{H}_2\text{O}_2:\text{H}_2\text{O}$, 22%:9%:69% in volume.

2.1 Polystyrene nanospheres lithography PSNS

are commonly utilised in phase separation processes. Recently these particles have been used to form self-assembled masks for nanolithography on large area [8–11].

In general, heterophase polymerizations [12] are the techniques of election for the preparation of these and other colloids, including a variety of different processes like suspension, dispersion, emulsion [13] as well as nanoemulsion polymerizations [14, 15].

Self-assembly is the natural alternative to top-down fabrication at the nanoscale. The top-down approach of semiconductor industry has severe limitations under the dimension of 100 nm, because optical lithography, the widest technology used to define in parallel geometries and patterns, is affected by diffraction problems under 500 nm for the UV light. Higher energy radiations and liquid immersion lithography can be used to push down the resolution to 190 nm, but often sequential methods, like Electron or Ion Beam Lithography, are adopted, leaving the application and design of small geometries at the nanoscale on a large areas unresolved.

Self-assembly is a parallel process where from a disordered system the order appears and is strictly related to the control of size, shape and surface properties of the building blocks, like charge, hydrophobicity and functionality. These properties manage the attractive and repulsive forces among the building blocks so being responsible for the self-assembly.

Energy minimization, without external influence, drives the self-assembly of building blocks to form structures in static equilibrium.

2.2 Formation of 2D arrays of colloidal spheres

Monodispersions of nanospheres can be assembled in ordered 2D crystals and arrays on solids or thin films with several methods [16–19], the most common being on a liquid surface by attractive long-range interactions, in a thin film of liquid spread on a solid using attractive capillary forces or via electrophoretic deposition on the surface of a solid electrode.

We used the first method, forming the 2D crystal of spheres on the air–liquid interface and then lifting it on the surface of a solid substrate. The spreading on the water surface is rather critical, since the monodispersions of nanospheres are charged with surfactant groups (typ. SO_4^-) and a fast diffusion of the nanospheres occurs on the liquid. To counterbalance these repulsive forces, a spreading agent, typically alcohol, is added to the monodispersion, in 1:1 or 1:2 ratio. This allows a different floating level on the water surface to be reached, thus screening the repulsive contributes with dipoles induced by the molecules of liquid [20–22]. To facilitate the aggregation in a big crystal, even if composed of domains with different orientations, an anionic surfactant (sodium dodecil sulphate, 5 vol%) can be added at the water surface, repulsing and compacting the various floating crystals. With this method, a number of parameters like alcohol content, surface hydrophobicity, initial charge density on nanospheres and physico-chemical properties of the liquid and spreading conditions on the air–liquid surface are crucial for the self-assembly of large 2D floating crystals.

2.3 Sputter etching After self-assembly of nanospheres, and subsequent lifting on a silicon substrate and drying, the samples were sputter-etched at a power of 100 W and 10^{-2} mbar of Ar for 1 min. This etching works as a localized indentation of the silver layer, since the Ar^+ ions can reach the thin metal film only at the interstitial sites among the spheres, obtaining this way an array of nanoindentations in hcp geometry.

2.4 Metal-assisted etching MAE has been recently proposed by Bohn and coworker [23]. The preferred materials for this kind of etching are the noble metals like Au, Ag and Pt, but other metals can be in principle used, like Co and magnetic alloys, with the limitation of low etch rates due to the dissolution of these metals in HF.

MAE is a sort of self-catalytic etching of silicon and other semiconductors, with no need of polarization, differently from electrochemical etching. The formation mechanism is in fact ruled by local redox potential of the metal respect to silicon, driving the holes necessary to dissolution at the metal–semiconductor interface. Metals can be deposited in form of thin solid films, or by precipitation starting from liquid metallic salts like AgNO_3 and others.

The metal clusters at the surface of the silicon wafer, rapidly sink following the crystallographic directions, and define silicon walls or wires, depending on the metal particle distribution at surface, the sample temperature and the concentration of the etchants. In our case, since the metal

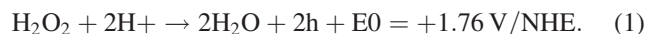
is patterned on the surface, MAE leads to regular morphologies.

The dissolution of silicon in HF and an oxidizing agent like hydrogen peroxide is a combination of chemical and electroless process, having strong similarities with porous silicon formation or electropolishing by stain etching in HF-HNO₃.

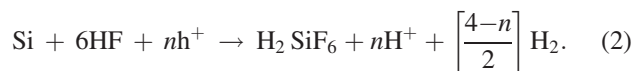
In electrochemical silicon etching, currents flow from anode to cathode sites, and the two or four holes are required for silicon atom removal, depending if the regime is porous silicon formation or electropolishing. In the case of MAE, holes are injected in silicon by H₂O₂, independently from the original substrate doping. In this case, the oxidizing agent concentration plays the role of current density in electrochemical processes. HF concentration rules dissolution and surface chemistry at the same way for both the processes. The ratio between oxidizing agent and HF deeply affects the etching regimes and the morphologies.

The silver clusters at the silicon surface are charged with electrons that, due to charge compensation, tend to localize holes at silicon-silver interface. The majority of these holes are produced by H₂O₂ dissociation at cathode in presence of catalyzing silver, as shown in Eq. (1) and forming SiO₂ or removing Si at anode, as in Eq. (2).

2.4.1 Cathodic reaction The Ag particles at the cathode, catalyze the reduction of H₂O₂ as in Eq. (1) taking advantage from a favourable redox potential, and enhancing the etch rates by supplying free holes in proximity of Si-Ag interface.

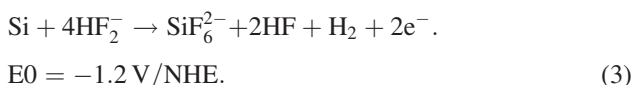


2.4.2 Anodic reaction In analogy to the chemical dissolution of Si in HF-HNO₃ [24, 25] summarizing the different mechanisms proposed in the literature [26] and following the work of Chartier and coworkers [7], the anodic reaction is proposed as:



The general form is valid for porous silicon formation and electropolishing, where *n*, ranging from 2 to 4, is the number of holes per dissolved Si atom.

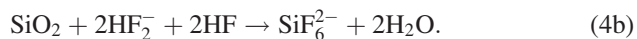
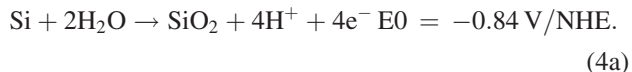
In the case of *n* = 2, porous silicon formation occurs, with the following overall dissolution anodic reaction:



well below the critical current density of electropolishing (JPS) and also valid for HF/HNO₃ stain etching

In the case of *n* = 3, ½ H₂ per dissolved silicon atom, as in the case of 6 M HF – 6 M HNO₃ solutions [26] or in stable electrochemical dissolution at JPS [27].

The electropolishing regime occurs when *n* = 4, as for low HF/HNO₃ ratio or for current densities higher than JPS, with a different mechanism involving the formation and dissolution of intermediate species like SiO₂ and without H₂ formation (4a, 4b).



3 Discussion The morphologies resulting from MAE are deeply affected by the distribution of metal particles on the silicon surface, so the use of PSNS self-assembly and MAE is rather interesting for application fields requiring a large-area nanostructuring, like sensors, anti-reflection layers in photovoltaics, functional materials and surfaces. Recently, Gösele and coworkers [28] used a mask of self-assembled PSNS to grow ordered pillars and wires by means of MBE. Our method allows for higher aspect ratios, with more affordable equipment.

Figure 2 shows the extruded array of SiNWs resulting from 30 s of MAE. Ordered areas of nanowires with average diameter around 30 and 300 nm long are evident in the SEM micrograph (detail in Fig. 5).

The geometry of the wires is in general triangular or polygonal, determined by the shape of the silver area removed by the argon ion bombardment. Different silver thicknesses have been used, 20, 30 and 40 nm, the best results outcome from the 30 nm thin films. In the case of 20 nm and less, in fact, undesired wires are forming among the metal grains of silver, and with 40 nm the metal layer tends to delaminate during etching in HF:H₂O₂. The ideal thickness obviously depends on the quality of the deposition method.

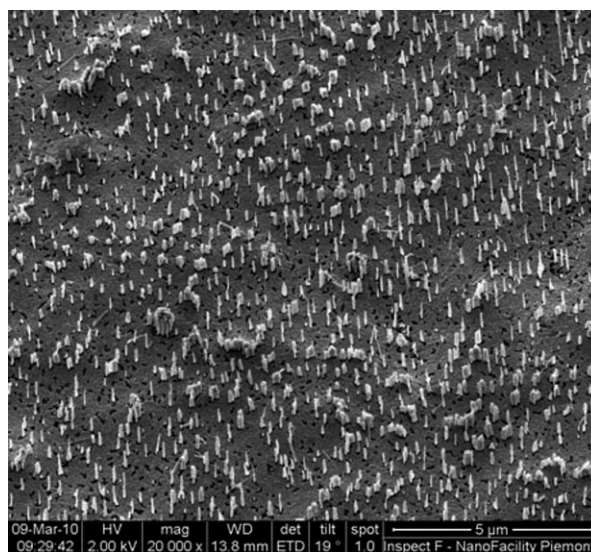


Figure 2 Ordered areas of SiNWs obtained through the process described in Fig. 1.

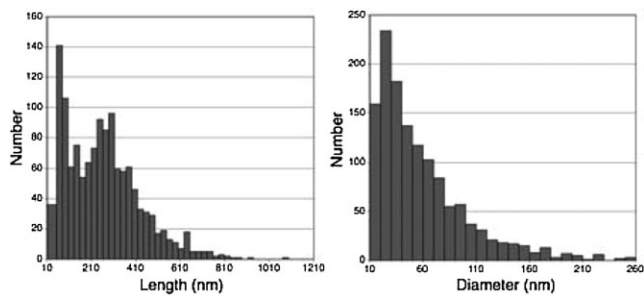


Figure 3 Distribution of nanowire lengths and diameters along the array, as calculated by means of morphological analysis software.

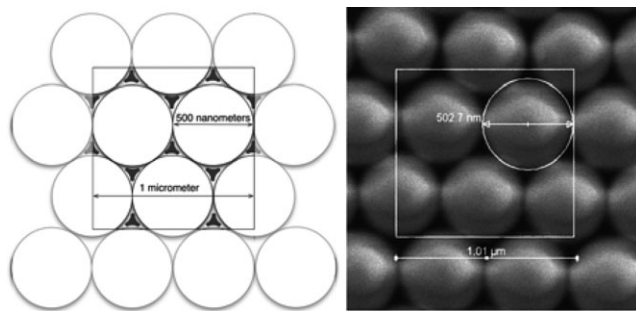


Figure 4 Left: scheme of the ideal nanowire density per square micrometer (10 wires per square micron), as allowed by geometrical factors in the hexagonal close packing of 500 nm spheres. Right: the corresponding SEM micrograph of the assembly.

For thermal evaporation, the metal grains are still separated even for higher thickness, while for high vacuum sputtered metal films the growth tends to be epitaxial and the metal clusters are more compact.

The density along the array is determined by the hcp configuration, as shown in Fig. 4, and verified in Fig. 5, with 500 nm spheres assembly, only 10 interstitial sites per a square unit cell of $1 \mu\text{m}$ are possible, extruding 10 wires during MAE.

In Fig. 3, the nanowire length and diameter distributions along the array are shown. This analysis has been carried out by using a shareware code for microscopy and morphological analysis, Image J, from NIH [29]. The diameter distribution appears to be a log-normal, typical of size dispersion in other nanostructured materials like porous silicon. The average is around 30 nm, and a possible data loss under 10 nm is possible due to SEM resolution and image processing tools, minimum pixel dimension limit.

The nanowire length distribution is not so trivial to be interpreted, showing a more complicate shape, with two different peaks around 300 and 40 nm. In particular, the last peak could be related to nanowire breaking or to an incomplete extrusion of the SiNW due to an inefficient removal of the silver layer by the sputter etching process. The small area of the shorter wires seems to indicate this possible reason. It must be remarked that the etching front is not completely homogeneous on the millimeter scale, and,

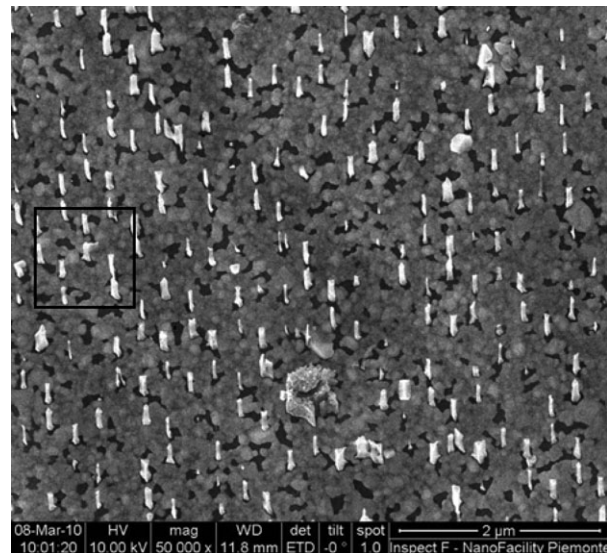


Figure 5 Closer view of the SiNWs. In this microphotograph the hcp arrangement due to the self-assembly of PSNS is evident. The black square on the left is one square micrometer, and the density of 10 SiNWs per $1 \mu\text{m}^2$ is obtained, confirming the ideal scheme of Fig. 5.

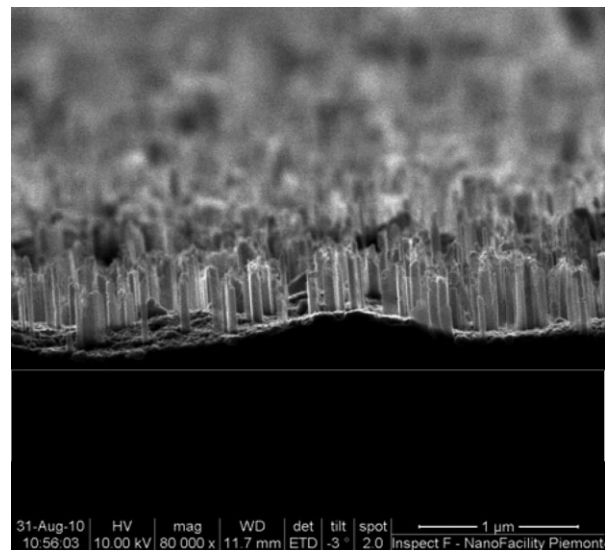


Figure 6 Cross section of the SiNWs array. A modulation in the etching front is clearly visible.

different heights of SiNWs are observed. This is probably due to the difficulty encountered by the etching solution to reach the interface between silver and silicon. Another aspect that could affect the homogeneity of the nanowire array is the hydrogen bubbling during silicon etching, affecting the array homogeneity on large scale. An additional effect is clearly visible in Fig. 6, as a sort of waviness in the etching front, also observed in porous silicon formation, and increasing with porous layer thickness. Work on different metals, like gold, and varying density and wettability of the etching solution, is in progress to ascertain this effect.

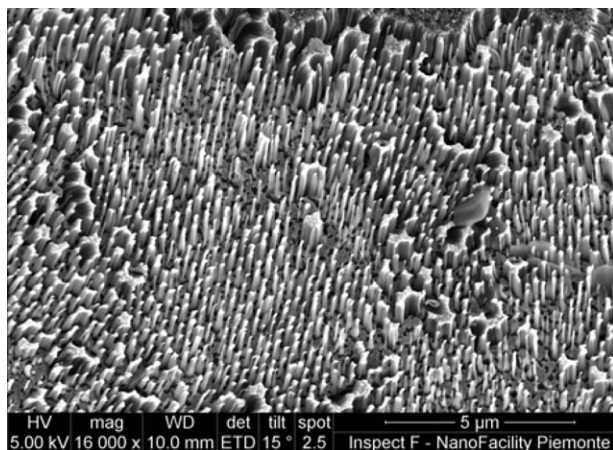


Figure 7 Ordered area of SiNWs as reported in Figs. 3 and 5, with longer etching times (60 s), resulting in longer SiNWs.

Despite the above described effects of the etching front modulation, the average extension of the areas where the morphological characteristics of the wires is rather large, this modulation affects mainly the length distribution over extensions of millimetres. The nanospheres self-assembly structure, influences only the order and the orientation of the wires, not the dimensions. The spheres in fact, tend to arrange in clusters of different orientation (see Fig. 7) of typical sizes ranging from few micrometers to 50–100 μm of side. These domains with single orientation are separated by linear defects. After MAE, these dislocations give origin to non-separate wires, so forming walls delimiting the domains. Inside the different domains the wires are rather homogeneous, in terms of diameter and length. The array orientation varies from zone to zone, exhibiting different 2D lattice orientation, reflecting the original disposition of the nanospheres.

The distance between nanowires is closely related to the sphere diameters, as expected, but under 100 nm the rapid etching rates are source of disorder. A dedicate and accurate choice of the etching parameters has still to be found. Work is in progress to get results on these small diameters.

Increasing etching times, longer wires have been obtained, as in Fig. 7, where a sample obtained by the same procedure of the previous is shown, but an etching time of 60 s has been used. For longer times of etching an erosion of the nanowire top has been observed due to pure chemical dissolution in HF, and collapsing and sticking among groups of wires is rather common, unless supercritical drying methods are used.

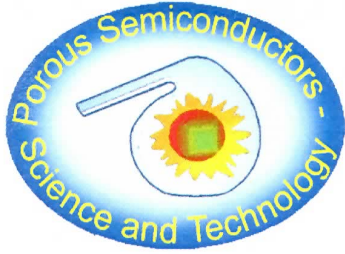
In conclusion, ordered arrays of SiNWs have been designed and fabricated with the combination of two techniques, self-assembly and MAE.

The simple variation of times during nanoindentation by sputter etching and during MAE, offers an easy and repeatable control of nanowires size and length, maintaining the order and the geometry introduced by nanospheres self-assembly.

Acknowledgements This work has been performed at NanoFacility Piemonte, INRiM, a laboratory supported by Compagnia di San Paolo.

References

- [1] Y. Li, F. Qian, J. Xiang et al., *Mater. Today* **9**, 18 (2006).
- [2] M. Menon, D. Srivastava, I. Ponomareva et al., *Phys. Rev. B* **70**, 12 (2004).
- [3] T. Bozhi, X. Zheng, T. J. Kempa, Y. Fang, N. Yu, G. Yu, J. Huang, and C. M. Lieber, *Nature* **449**, 885 (2007).
- [4] L. Qu, Y. Li, H. Zhang, Y. Huang, and X. Duan, *Nano Lett.* **9**, 4539 (2009).
- [5] B. J. Alemn, K. E. Fischer, S. L. Tao, R. H. Daniels, E. M. Li, M. D. Bnger, G. Nagaraj, P. Singh, A. Zettl, and T. A. Desai, *Nano Lett.* **9**, 716 (2009).
- [6] S. Chattopadhyay, Xiuling. Li, and P. W. Bohn, *J. Appl. Phys.* **91**, 6134 (2002).
- [7] S. Bastide, C. Chartier, and C. Levy-Clement, *Electrochim. Acta* **53**, 5509 (2008).
- [8] H. W. Deckman and J. H. Dunsmir, *Appl. Phys. Lett.* **41**, 377 (1982).
- [9] M. Giersig and P. Mulvaney, *Langmuir* **9**, 3408 (1993).
- [10] H. W. Deckman and J. H. Dunsmuir, *Appl. Phys. Lett.* **4**, 377 (1982).
- [11] J. C. Hulteenand and R. P. Van Duyne, *J. Vac. Sci. Technol. A* **13**, 1553 (1995).
- [12] M. Antonietti and K. Tauer, *Macromol. Chem. Phys.* **204**, 207 (2003).
- [13] C. S. Chern, *Prog. Polym. Sci.* **31**, 443 (2006).
- [14] C. Solans, P. Izquierdo, J. Nolla, N. Azemar, and M. J. Garcia-Celma, *Curr. Opin. Colloid Interf. Sci.* **10**, 102 (2005).
- [15] J. M. Asua, *Prog. Polym. Sci.* **27**, 1283 (2002).
- [16] C. A. Murray and D. H. V. Winkle, *Phys. Rev. Lett.* **58**, 1200 (1987).
- [17] A. T. Skjeltorp and P. Meakin, *Nature* **335**, 424 (1988).
- [18] N. D. Denkov, O. D. Velev, P. A. Kralchevsky, I. B. Ivanov, H. Yoshimura, and K. Nagayama, *Nature* **361**, 26 (1993).
- [19] G. Picard, *Langmuir* **14**, 3710 (1998).
- [20] A. J. Hurd and D. W. Schaefer, *Phys. Rev. Lett.* **54**, 1043 (1985).
- [21] Z. Horvolgyi, M. Mate, and M. Zrinyi, *Colloids Surf. A: Physicochem. Eng. Asp.* **84**, 207 (1994).
- [22] H. H. Wickman and J. N. Korley, *Nature* **393**, 445 (1998).
- [23] X. Li and P. W. Bohn, *Appl. Phys. Lett.* **77**, 2572 (2000).
- [24] H. Robbins and B. Schwartz, *J. Electrochem. Soc.* **123**, 1903 (1976).
- [25] E. S. Kooij, K. Butter, and J. J. Kelly, *Electrochem. Solid State Lett.* **2**, 178 (1999).
- [26] M. Winzer, M. Kleiber, N. Dix, and R. Wiesendanger, *Appl. Phys. A* **63**, 617 (1996).
- [27] V. Lehmann, *Electrochemistry of Silicon* (WILEY-VCH Verlag GmbH, Weinheim, 2002), p. 58.
- [28] B. Fuhrmann, H. S. Leipner, H. R. Höche, L. Schubert, P. Werner, and U. Gösele, *Nano Lett.* **5**, 2524 (2005).
- [29] ImageJ, National Institutes of Health, USA. <http://rsb.info.nih.gov/ij>.



PSST - 2012
Málaga, 25-30th March

BEST POSTER OF THE DAY

Title:

Submicron machining and biomolecules immobilization on porous silicon by electron beam lithography

By:

D. Imbraguglio, A. M. Giovannozzi, A. Nastro, A. M. Rossi

Chosen as the best Poster presented on March 28th

Prof. L. Canham Prof. A. Cantarero Prof. N. Koshida Prof. M. Sailor

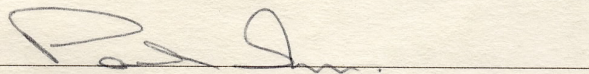
euspen | challenge 2012

This certificate is presented to

Mr Dario Imbraguglio

Most Innovative Concept

Proudly sponsored by Heidenhain GmbH



Prof. Paul Shore
euspen President

20th July 2012

Date



HEIDENHAIN